soft-tissue sarcomas (9, 10). Telomerase activation is closely correlated with the expression of the human telomerase reverse transcriptase (*hTERT*) gene (11). On the basis of these data, we previously developed a telomerase-specific replication-competent oncolytic adenovirus OBP-301 (Telomelysin) in which the *hTERT* gene promoter drives the expression of the *E1A* and *E1B* genes (12). A phase I clinical trial of OBP-301, which was conducted in the United States on patients with advanced solid tumors, indicated that OBP-301 was well tolerated by patients (13). Recently, we reported that OBP-301 efficiently killed human bone and soft-tissue sarcoma cells (14, 15). However, some osteosarcoma cell lines were not sensitive to the antitumor effect of OBP-301. Therefore, to efficiently eliminate tumor cells with OBP-301, its antitumor effects need to be enhanced.

Cancer gene therapy is defined as the treatment of malignant tumors via the introduction of a therapeutic tumor suppressor gene or the abrogation of an oncogene. The tumor suppressor *p53* gene has an attractive tumor suppressor profile as a potent therapeutic transgene for induction of cell-cycle arrest, senescence, apoptosis, and autophagy (16). Dual cell death pathways, such as apoptosis and autophagy, induced by p53 transactivation are mainly involved in the suppression of tumor initiation and progression. However, among the p53 downstream target genes, p21, which is most rapidly and strongly induced during the DNA damage response, mainly induces cell-cycle arrest through suppression of apoptotic and autophagic cell death pathways (17, 18). Thus, p21 suppression may be a more effective strategy for the induction of apoptotic and autophagic cell death pathways in tumor cells, particularly when the tumor suppressor *p53* gene is overexpressed in tumor cells in response to cancer gene therapy.

A p53-expressing replication-deficient adenovirus (Ad-p53, Advexin) has previously been reported to induce an antitumor effect in the *in vitro* and *in vivo* settings (19, 20) as well as in some clinical studies (21–24). We recently reported that combination therapy with OBP-301 and Ad-p53 resulted in a more profound antitumor effect than monotherapy with either OBP-301 or Ad-p53 (25). Moreover, we generated armed OBP-301 expressing the wild-type *p53* tumor suppressor gene (OBP-702) and showed that OBP-702 suppressed the viability of various types of epithelial malignant cells more efficiently than did OBP-301 (26). OBP-702 induced a more profound apoptotic cell death effect than Ad-p53, likely via adenoviral E1A-mediated suppression of anti-apoptotic p21 in human epithelial malignant cells. However, it remained unclear whether OBP-702 efficiently induces an antitumor effect in human nonepithelial malignant cells, including osteosarcomas.

In the present study, we investigated the *in vitro* cytopathic efficacy of the p53-expressing telomerase-specific replication-competent oncolytic adenovirus, OBP-702, in human osteosarcoma cells, and we compared the induction level of apoptotic and autophagic cell deaths in OBP-301–resistant human osteosarcoma cells infected with OBP-301, OBP-702, and Ad-p53. The molecular mechanism by which OBP-702 mediates induction of apoptosis and autophagy was also investigated. Finally, the *in vivo* antitumor effect of OBP-702 was evaluated using an orthotopic OBP-301–resistant human osteosarcoma xenograft tumor model.

## Materials and Methods

### Cell lines

The human osteosarcoma cell lines, HOS and SaOS-2, were kindly provided by Dr. Satoru Kyo (Kanazawa University, Ishikawa, Japan). These cells were propagated as monolayer cultures in Dulbecco's Modified Eagle's Medium. The human osteosarcoma cell line, U2OS, was obtained from the American Type Culture Collection and was grown in McCoy's 5a Medium. The human osteosarcoma cell line, MNNG/HOS, was purchased from DS Pharma Biomedical and was maintained in Eagle's Minimum Essential Medium containing 1% nonessential amino acids. All media were supplemented with 10% FBS, 100 U/mL penicillin, and 100 mg/mL streptomycin. The normal human lung fibroblast (NHLF) cell line, NHLF, was obtained from TaKaRa Biomedicals. NHLF cells were propagated as monolayer culture in the medium recommended by the manufacturer. Although cell lines were not authenticated by the authors, cells were immediately expanded after receipt and stored in liquid $N_2$. Cells were not cultured for more than 5 months following resuscitation. The cells were maintained at 37°C in a humidified atmosphere with 5% $CO_2$.

### Recombinant adenoviruses

The recombinant telomerase-specific replication-competent adenovirus OBP-301 (Telomelysin), in which the promoter element of the *hTERT* gene drives the expression of *E1A* and *E1B* genes, was previously constructed and characterized (12, 27). For OBP-301–mediated induction of exogenous *p53* gene expression, we recently generated OBP-702, in which a human wild-type *p53* gene expression cassette was inserted into the *E3* region (Supplementary Fig. S1; ref. 26). Ad-p53 is a replication-defective adenovirus serotype 5 vector with a *p53* gene expression cassette at the *E1* region (19, 20). Recombinant viruses were purified by ultracentrifugation using cesium chloride step gradients, their titers were determined by a plaque-forming assay using 293 cells and they were stored at −80°C.

### Cell viability assay

Cells were seeded on 96-well plates at a density of $1 \times 10^3$ cells/well 24 hours before viral infection. All cell lines were infected with OBP-702 at multiplicity of infections (MOI) of 0, 0.1, 1, 10, 50, or 100 plaque-forming units (PFU)/cell. Cell viability was determined on days 1, 2, 3, and 5 after virus infection using Cell Proliferation Kit II (Roche Molecular Biochemicals). The 50% inhibiting dose ($ID_{50}$) value of OBP-702 for each cell line was calculated

using cell viability data obtained on day 5 after virus infection.

### Time-lapse confocal laser microscopy

GFP-expressing MNNG/HOS (MNNG/HOS-GFP) cells were established by stable transfection with GFP expression plasmid using Lipofectamine LTX (Invitrogen). MNNG/HOS-GFP and NHLF cells were seeded in 35-mm glass-based dishes at a density of $1 \times 10^5$ cells/dish 24 hours before infection and were infected with OBP-702 at an MOI of 10 PFU/cell for 72 hours. Phase-contrast and fluorescence time-lapse recordings were obtained to concomitantly analyze cell morphology and GFP expression using an inverted FV10i confocal laser scanning microscopy (OLYMPUS).

### Western blot analysis

SaOS-2 and MNNG/HOS cells, seeded in a 100-mm dish at a density of $1 \times 10^5$ cells/dish, were infected with OBP-301, OBP-702, or Ad-p53 at the indicated MOIs. In contrast, SaOS-2 cells were transfected with 10 nmol/L *miR-93* (Ambion), *miR-106b* (Ambion), or control miRNA (Ambion) 24 hours before Ad-p53 infection and infected with Ad-p53 at an MOI of 100 for 48 hours. Whole-cell lysates were prepared in a lysis buffer [50 mmol/L Tris-HCl (pH 7.4), 150 mmol/L NaCl, 1% Triton X-100] containing a protease inhibitor cocktail (Complete Mini; Roche) at the indicated time points. Proteins were electrophoresed on 6% to 15% SDS-PAGE and were transferred to polyvinylidene difluoride membranes (Hybond-P; GE Health Care). Blots were blocked with 5% non-fat dry milk in TBS-T (Tris-buffered saline and 0.1% Tween-20, pH 7.4). The primary antibodies used were: rabbit anti-PARP polyclonal antibody (pAb; Cell Signaling Technology), mouse anti-p53 monoclonal antibody (mAb; Calbiochem), mouse anti-$p21^{WAF1}$ mAb (Calbiochem), rabbit anti-E2F1 pAb (Santa Cruz Biotechnology), mouse anti-Ad5 E1A mAb (BD PharMingen), rabbit anti-microtubule-associated protein 1 light chain 3 (LC3) pAb [Medical & Biological Laboratories (MBL)], mouse anti-p62 mAb (MBL), rabbit anti-damage-regulated autophagy modulator (DRAM) pAb (Abgent), and mouse anti-β-actin mAb (Sigma-Aldrich).

### Flow cytometric analysis

To analyze the active caspase-3 expression, cells were incubated for 20 minutes on ice in Cytofix/Cytoperm solution (BD Biosciences), labeled with phycoerythrin (PE)-conjugated rabbit anti-active caspase-3 mAb (BD Biosciences) for 30 minutes, and then analyzed using FACS array (BD Biosciences).

To evaluate the sub-$G_1$ population, which is a apoptosis indicator, in SaOS-2 cells after virus infection, SaOS-2 cells were seeded in a 100-mm dish at a density of $1 \times 10^6$ cells/dish 24 hours before viral infection and were infected with mock, OBP-301, Ad-p53, or OBP-702 at an MOI of 10 PFUs/cell for 48 hours. Cells were trypsinized and resuspended in original supernatant to ensure that both attached and nonattached cells were analyzed. Cells stained with propidium iodide were analyzed using FACS array (BD Biosciences).

### Quantitative real-time reverse transcription PCR analysis

To evaluate the expressions of *miR-93* and *miR-106b* in tumor cells after OBP-702 infection, SaOS-2 and MNNG/HOS cells were seeded on 6-well plates at a density of $2 \times 10^5$ cells/well 24 hours before viral infection and were infected with OBP-702 at MOIs of 0, 1, 5, 10, 50, or 100 PFU/cell. Three days after virus infection, total RNA was extracted from the cells using a miRNeasy Mini Kit (Qiagen). The concentration and quality of RNA were assessed using a Nanodrop spectrophotometer. cDNA was synthesized from 10 ng of total RNA using the TaqMan MicroRNA Reverse Transcription Kit (Applied Biosystems), and quantitative real-time reverse transcription (RT)-PCR was carried out using the Applied Biosystems StepOnePlus real-time PCR System. The expressions of *miR-93* and *miR-106b* were defined from the threshold cycle ($C_t$), and relative expression levels were calculated using the $2^{-\Delta\Delta C_t}$ method after normalization with reference to the expression of U6 small nuclear RNA.

### *In vivo* orthotopic MNNG/HOS xenograft tumor model

Animal experimental protocols were approved by the Ethics Review Committee for Animal Experimentation of Okayama University School of Medicine (Okayama, Japan). MNNG/HOS cells ($5 \times 10^6$ cells per site) were inoculated into the tibias of female athymic nude mice aged 6 to 7 weeks (CLEA Japan). Palpable tumors developed within 21 days and were permitted to grow to approximately 5 to 6 mm in diameter. At that stage, a 50-μL volume of solution containing OBP-702, OBP-301, or Ad-p53 at a dose of $1 \times 10^8$ PFU or PBS was injected into the tumors for 3 cycles every 2 days. Tumor volume was monitored by computed tomographic (CT) imaging once a week after virus infection.

### Three-dimensional computed tomography imaging

The tumor volume and formation of osteolytic lesions were evaluated using three-dimensional CT (3D-CT) imaging (ALOKA Latheta LCT-200; Hitachi Aloka Medical). The tumor volume was calculated by INTAGE Realia software (Cybernet Systems).

### Histopathologic analysis

Tumors were fixed in 10% neutralized formalin and embedded in paraffin blocks. Sections were stained with hematoxylin/eosin and analyzed by light microscopy.

### Statistical analysis

Data are expressed as means ± SD. Student *t* test was used to compare differences between groups. Statistical significance was defined as $P < 0.05$.

## Results

### *In vitro* cytopathic efficacy of OBP-702 against human osteosarcoma cell lines

To evaluate the *in vitro* cytopathic activity of OBP-702, we used the 2 OBP-301–sensitive human osteosarcoma cells (HOS and U2OS) and the 2 OBP-301–resistant human osteosarcoma cells (SaOS-2 and MNNG/HOS) that were recently described (14). The cell viability of each cell was assessed over 5 days after infection using the XTT assay. OBP-702 infection suppressed the viability of OBP-301–sensitive and -resistant cells in dose- and time-dependent manners (Fig. 1A and B). When the $ID_{50}$ values of OBP-702 in all 4 human osteosarcoma cells were compared with those of OBP-301 calculated in a previous report (14), all cell lines were more sensitive to OBP-702 than to OBP-301 (Table 1). The $ID_{50}$ values of OBP-702 were also lower than those of Ad-p53 (Supplementary Fig. S2). However, OBP-702 did not exhibit any cytopathic effect in NHLF cells (Fig. 1B). When GFP-expressing MNNG/HOS-GFP cells were cocultured with human normal NHLF cells, OBP-702 infection showed a cytopathic effect (confirmed by observation of round-shaped morphologic changes) in MNNG/HOS-GFP cells but not in NHLF cells (Fig. 1C). These results indicate that OBP-702 was more cytopathic than OBP-301 for human osteosarcoma cells but was not cytopathic for normal human cells.

### Increased induction of apoptosis by OBP-702 when compared with OBP-301 or Ad-p53

We next investigated whether OBP-702 induces more profound apoptosis when compared with OBP-301 or Ad-p53. OBP-301–resistant SaOS-2 and MNNG/HOS cells

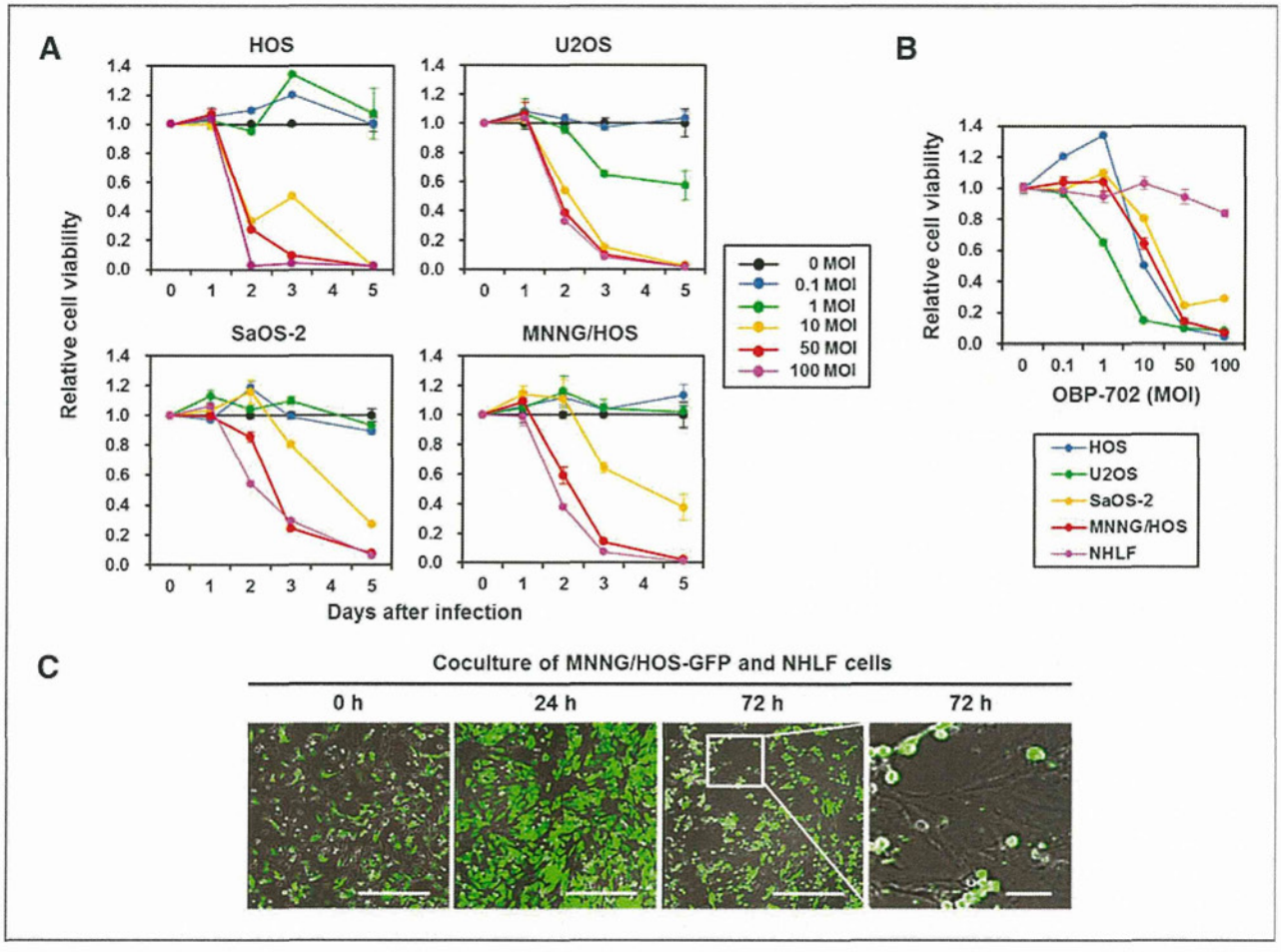


Figure 1. *In vitro* cytopathic effect of OBP-702 in human osteosarcoma cell lines. A, OBP-301–sensitive (HOS and U2OS) and OBP-301–resistant (SaOS-2 and MNNG/HOS) human osteosarcoma cells were infected with OBP-702 at the indicated MOI, and cell viability was quantified over 5 days using the XTT assay. Cell viability was calculated relative to that of the mock-infected group on each day, which was set at 1.0. Cell viability data are expressed as mean values ± SD ($n = 5$). B, four human osteosarcoma cells and one normal fibroblast NHLF cell were seeded 24 hours before viral infection and were infected with OBP-702 at the indicated MOIs, and cell viability was examined on day 5 using the XTT assay. Cell viability was calculated relative to that of the mock-infected group, which was set at 1.0. Cell viability data are expressed as mean ± SD ($n = 5$). C, time lapse images of cytopathic effect of OBP-702 in coculture of GFP-expressing MNNG/HOS cells with human normal fibroblast NHLF cells. MNNG/HOS-GFP cells coincubated with NHLF cells were recorded for 72 hours after OBP-702 infection at an MOI of 10. Three images on the left are low magnification and one image on the right is high magnification of the area outlined by a white square. Left scale bars, 100 μm. Right scale bar, 10 μm.

**Table 1.** Comparison of $ID_{50}$ values of OBP-301 and OBP-702 in various human osteosarcoma cell lines

| Cell lines | Sensitivity to OBP-301 | Cell type | Relative hTERT mRNA expression | $ID_{50}$ value[a] (MOI) | | Ratio[b] (OBP-702/ OBP-301) |
|---|---|---|---|---|---|---|
| | | | | OBP-301 | OBP-702 | |
| SaOS-2 | Resistant | ALT | Negative | 98.1 | 5.5 | 0.06 |
| MNNG/HOS | Resistant | Non-ALT | 1 | 97.3 | 6.7 | 0.07 |
| U2OS | Sensitive | ALT | 0.3 | 38.2 | 1.2 | 0.03 |
| HOS | Sensitive | Non-ALT | 4.3 | 43.0 | 4.5 | 0.10 |

[a]The $ID_{50}$ values of OBP-702 and OBP-301 were calculated from the data of XTT assay on day 5 after infection.
[b]The ratio was calculated from the division of the $ID_{50}$ value of OBP-702 by the $ID_{50}$ value of OBP-301.

were infected with OBP-702, OBP-301, or Ad-p53, and apoptosis was assessed by Western blot and flow cytometric analyses. Western blot analysis showed that SaOS-2 cells exhibited the cleavage of PARP after infection with OBP-702 (>5 MOIs) or Ad-p53 (>50 MOIs), whereas MNNG/HOS cells had the cleavage of PARP after infection with OBP-702 (>5 MOIs) but not Ad-p53 (Fig. 2A). In contrast, OBP-301 did not induce apoptosis (data not shown). Furthermore, flow cytometric analysis showed that OBP-702 infection (10 MOIs) significantly increased the percentage of apoptotic cells with active caspase-3 when compared with Ad-p53 or OBP-301 at same doses in SaOS-2 and MNNG/HOS cells (Fig. 2B and C). Cell-cycle analysis also showed that OBP-702 (10 MOIs) induced the highest percentages of sub-$G_1$ population in SaOS-2 cells when compared with Ad-p53 or OBP-301 at same doses (Fig. 2D). These results suggest that OBP-702 induces increased apoptosis when compared with Ad-p53 or OBP-301 in human osteosarcoma cells.

### p53 induction in human osteosarcoma cells infected with OBP-702

To investigate the molecular mechanism of OBP-702–induced apoptosis in human osteosarcoma cells, we evaluated p53 expression after OBP-702 infection in SaOS-2 (p53-null) and MNNG/HOS (p53-mutant) cells in which endogenous p53 expression level was confirmed by Western blot analysis (Supplementary Fig. S3). OBP-702 efficiently induced p53 expression in SaOS-2 and MNNG/HOS cells (Fig. 3A). The level of p53 expression was higher in OBP-702–treated cells than in Ad-p53–treated cells (Fig. 3A). Despite of OBP-702–induced high p53 expression, p53 downstream target p21 protein was induced only in Ad-p53–treated cells.

To investigate the effect of exogenous p53 overexpression in virus replication, we next compared the replication abilities of OBP-702 and OBP-301 in p53-null SaOS-2 cells by measuring the relative amounts of *E1A* copy numbers. The *E1A* copy number of OBP-702 was similar to that of OBP-301 in SaOS-2 cells (Supplementary Fig. S4). These results indicate that OBP-702 efficiently induces exogenous p53 expression without affecting p21 expression and virus replication in human osteosarcoma cells.

### OBP-702–mediated upregulation of *miR-93* and *miR-106b* suppresses p21 expression

Adenoviral E1A protein has been shown to activate E2F1 expression (28), which is a multifunctional transcription factor that regulates diverse cell fates through induction of many target genes, including small noncoding miRNAs (29). Recently, E2F1-inducible *miR-93* and *miR-106b* have been shown to suppress p21 expression in human cancer cells (30). Therefore, we sought to investigate whether OBP-702 induces expressions of E2F1 and E2F1-regulated miRNAs (*miR-93* and *miR-106b*). OBP-702 infection activated E2F1 expression along with E1A accumulation in SaOS-2 and MNNG/HOS cells (Fig. 3B). The expression levels of *miR-93* and *miR-106b* were increased in association with E2F1 activation in OBP-702–infected SaOS-2 and MNNG/HOS cells (Fig. 3C). In contrast, E1A-deleted Ad-p53 infection did not increase expressions of E2F1 and E2F1-regulated *miR-93* and *miR-106b* (data not shown). Next, we assessed whether upregulation of *miR-93* and *miR-106b* efficiently suppresses p21 expression induced by Ad-p53–mediated p53 overexpression. Ad-p53 infection at MOIs of 10 and 100 efficiently induced p21 expression at 48 hours after infection in SaOS-2 cells (Supplementary Fig. S5). When SaOS-2 cells were infected with Ad-p53 at an MOI of 100 for 48 hours, pretransfection with *miR-93*, *miR-106b*, or both efficiently suppressed Ad-p53–induced p21 expression (Fig. 3D). Interestingly, both *miR-93*- and *miR-106b*–transfected SaOS-2 cells showed the 1.5-fold increased expression of cleaved PARP (C-PARP) in consistency with remarkable p21 downregulation when compared with those transfected with control miR. However, the expression level of C-PARP was not increased in the *miR-93*- or *miR-106b*–transfected SaOS-2 cells, although transfection with *miR-93* or *miR-106b* moderately decreased p21 expression. These results suggest that OBP-702 suppresses p21 expression through E1A-dependent upregulation of both E2F1-inducible *miR-93* and *miR-106b* and contributes to induction of apoptosis.

### Increased induction of autophagy by OBP-702 when compared with OBP-301

Recently, we showed that oncolytic adenovirus OBP-301 mainly induces programmed cell death in association with autophagy rather than apoptosis in human tumor

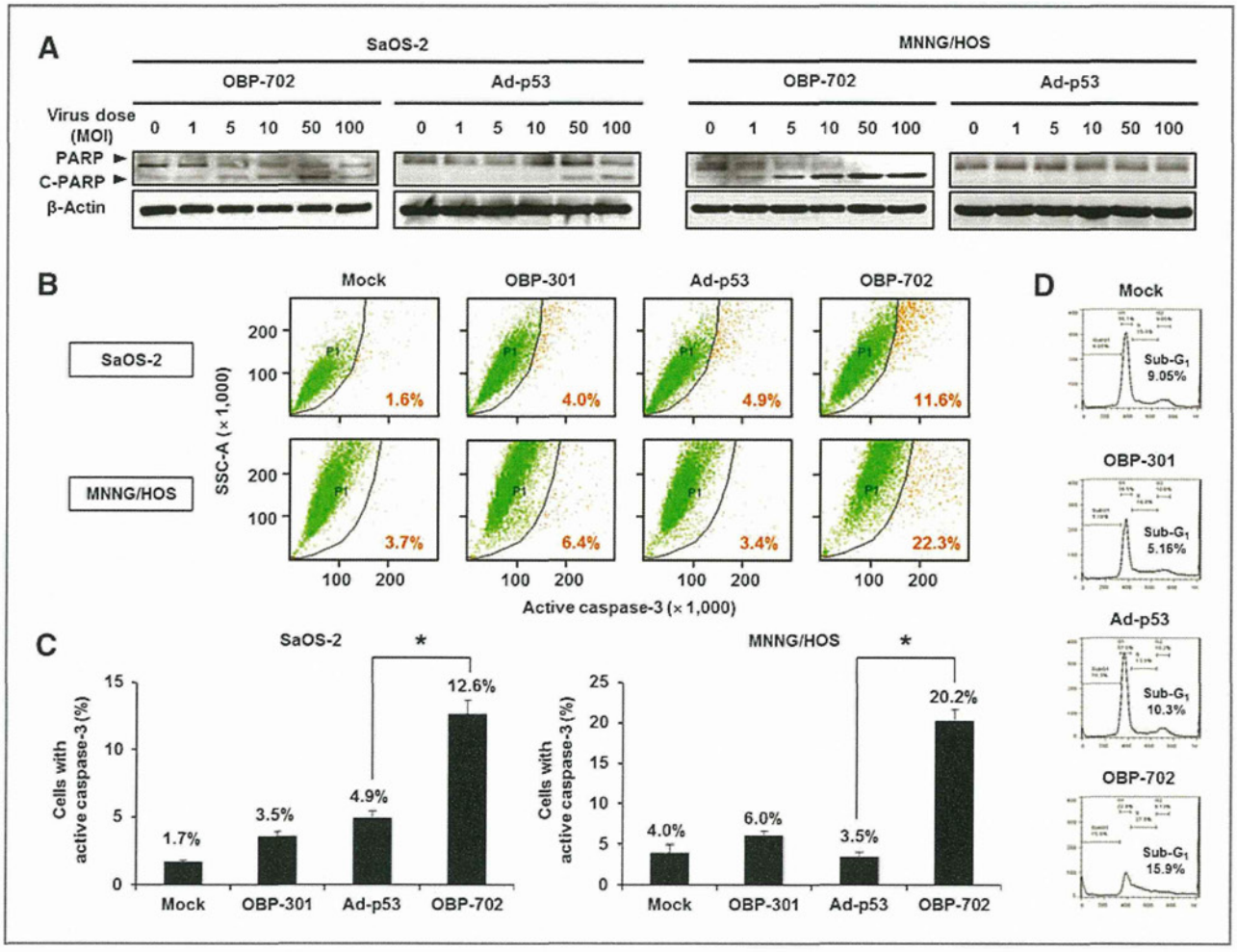


Figure 2. OBP-702 induces increased apoptosis when compared with OBP-301 or Ad-p53. A, OBP-301–resistant SaOS-2 and MNNG/HOS cells were infected with OBP-702 or Ad-p53 at the indicated MOIs for 72 hours. Cell lysates were subjected to Western blot analysis for the C-PARP and PARP. β-Actin was assayed as a loading control. B–D, SaOS-2 and MNNG/HOS cells were infected with OBP-702, OBP-301, or Ad-p53 at an MOI of 10 for 48 hours. Mock-infected cells were used as control. Caspase-3 activation was quantified using the flow cytometric analysis. Representative flow cytometric data are shown in B. The mean percentage of SaOS-2 cells and MNNG/HOS cells that express active caspase-3 was calculated on the basis of 3 independent experiments (C). The cell-cycle state was analyzed by flow cytometry in SaOS-2 cells after staining with propidium iodide. Representative cell-cycle data are shown (D). The percentage of sub-$G_1$ population was expressed in each graph. Bars, SD. Statistical significance was determined using Student *t* test. *, $P < 0.05$.

cells (31). Therefore, we next investigated whether OBP-702 induces more profound autophagy than does OBP-301. Western blot analysis revealed that OBP-702 infection showed increased autophagy, which was confirmed by conversion of LC3-I to LC3-II (increased ratio of LC3-II/LC3-I) and p62 downregulation, when compared with OBP-301 in MNNG/HOS cells (Fig. 4A). Moreover, the expression level of the p53-induced modulator of autophagy, DRAM (32), was decreased after OBP-301 infection, but its expression was maintained after OBP-702 infection (Fig. 4A). As p53-mediated p21 overexpression is known to inhibit both apoptosis and autophagy (17, 18), we further evaluated whether miR-mediated p21 suppression is involved in the enhancement of p53-mediated autophagy induction. Ad-p53–induced autophagy was enhanced by *miR-93*- and *miR-106b*–mediated p21 suppression (Fig. 4B). These results suggest that OBP-702 induces more profound autophagy than does OBP-301 and that this effect occurs via p53-mediated DRAM activation and miR-mediated p21 suppression.

### Enhanced antitumor effect of OBP-702 in an orthotopic xenograft tumor model

Finally, to assess the *in vivo* antitumor effect of OBP-702, we used an orthotopic MNNG/HOS tumor xenograft model. OBP-702, OBP-301, Ad-p53, or PBS were intratumorally injected for 3 cycles every 2 days. OBP-702 administration significantly suppressed tumor growth when compared with OBP-301, Ad-p53, or PBS in an orthotopic MNNG/HOS tumor model (Fig. 5A and B). 3D-CT examination revealed that OBP-702–treated tumors had less bone destruction than did OBP-301- or Ad-p53–treated

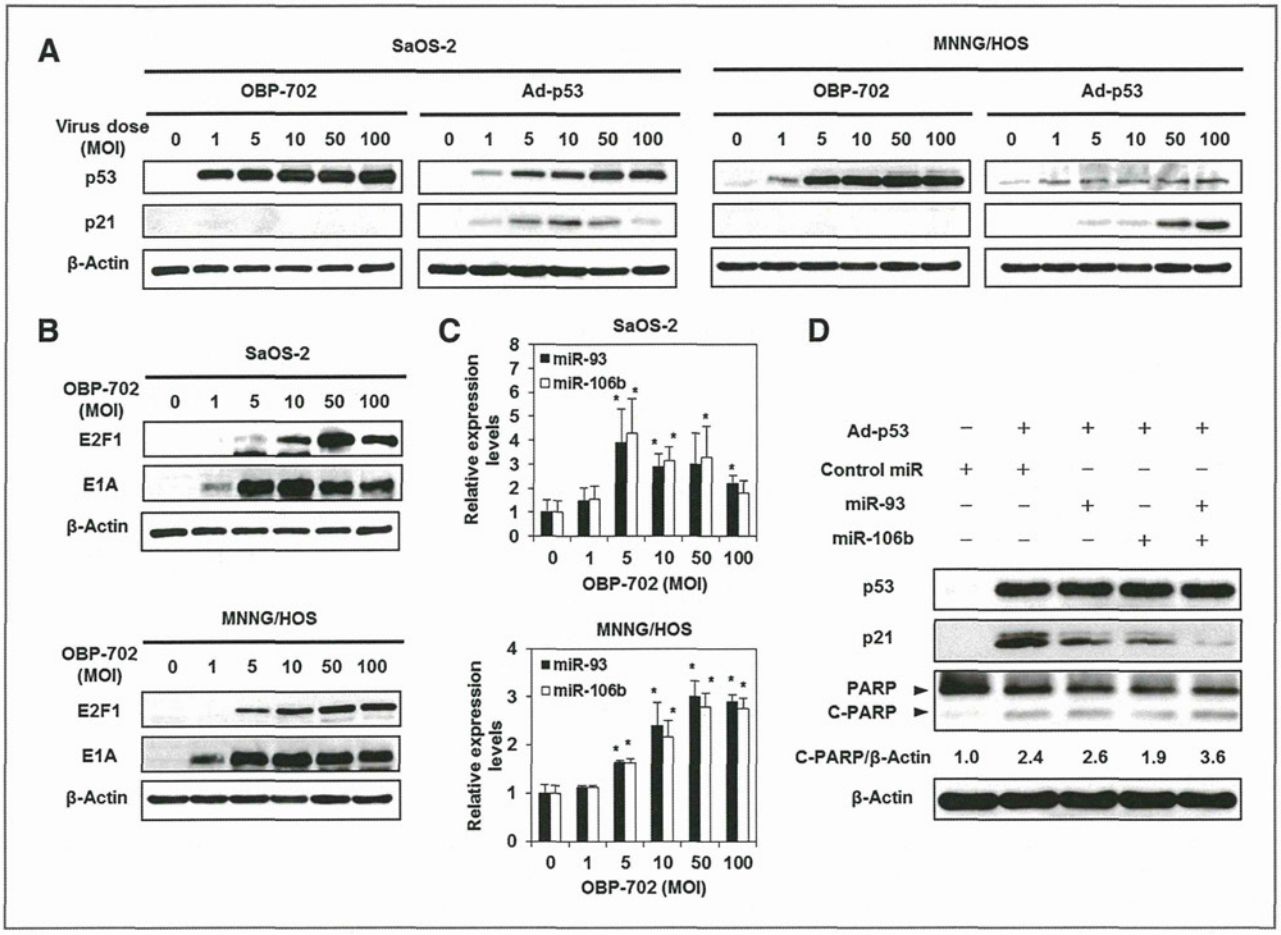


Figure 3. OBP-702 induces p53 overexpression with E1A-mediated p21 suppression via *miR-93* and *miR-106b* activation. A, expression of the p53 and p21 proteins in SaOS-2 and MNNG/HOS cells infected with OBP-702 or Ad-p53 at the indicated MOIs for 72 hours was assessed using Western blot analysis. B, expression of the E2F1 and viral E1A proteins in SaOS-2 and MNNG/HOS cells infected with OBP-702 at the indicated MOIs for 72 hours was assessed using Western blot analysis. C, expression of *miR-93* and *miR-106b* was assayed using qRT-PCR in SaOS-2 cells infected with OBP-702 at the indicated MOIs for 72 hours on 3 independent experiments. The values of *miR-93* and *miR-106b* at 0 MOI were set at 1, and the relative levels of *miR-93* and *miR-106b* at the indicated MOIs were plotted as fold induction. Bars, SD. Statistical significance was determined by Student *t* test. *, $P < 0.05$. D, SaOS-2 cells were transfected with 10 nmol/L *miR-93*, *miR-106*, or control miRNA 24 hours before Ad-p53 infection at an MOI of 100. At 48 hours after Ad-p53 infection, the expression levels of p53, p21, PARP, and C-PARP were examined by Western blot analysis. β-Actin was assayed as a loading control. By using ImageJ software, the expression level of C-PARP protein was calculated relative to its expression in the control miR–treated cells, whose expression level was designated as 1.0.

tumors (Fig. 5C). On histopathologic analysis, there were large necrotic areas in OBP-702–treated tumors but not in OBP-301- or Ad-p53–treated tumors (Fig. 5D). Moreover, the expression of the cell proliferation marker, Ki67, was also decreased, especially in OBP-702–treated tumor cells (Supplementary Fig. S6). These results suggest that OBP-702 eliminates tumor tissues more efficiently when compared with OBP-301 or Ad-p53.

## Discussion

We previously reported that telomerase-specific replication-competent oncolytic adenovirus OBP-301 has strong antitumor activity in a variety of human epithelial and nonepithelial malignant cells (12, 14, 27). However, some human osteosarcoma cells were resistant to the cytopathic activity of OBP-301 (14). In this study, we showed that a novel p53-expressing oncolytic adenovirus, OBP-702, had increased *in vitro* and *in vivo* antitumor effects than did OBP-301 in human osteosarcoma cells (Fig. 1 and 5). OBP-702 induced increased apoptosis in association with p53 upregulation and p21 downregulation when compared with replication-deficient Ad-p53 (Fig. 2 and 3A). E1A-dependent upregulation of *miR-93* and *miR-106b* was involved in OBP-702–mediated suppression of p21 expression (Fig. 3). Moreover, p53-mediated DRAM activation with p21 suppression enhanced oncolytic adenovirus-mediated autophagy induction (Fig. 4). Recent studies suggest that transgene-expressing armed oncolytic adenoviruses are a promising antitumor strategy for induction of oncolytic and transgene-induced cell death (33). Although p53 overexpression has been shown to enhance antitumor

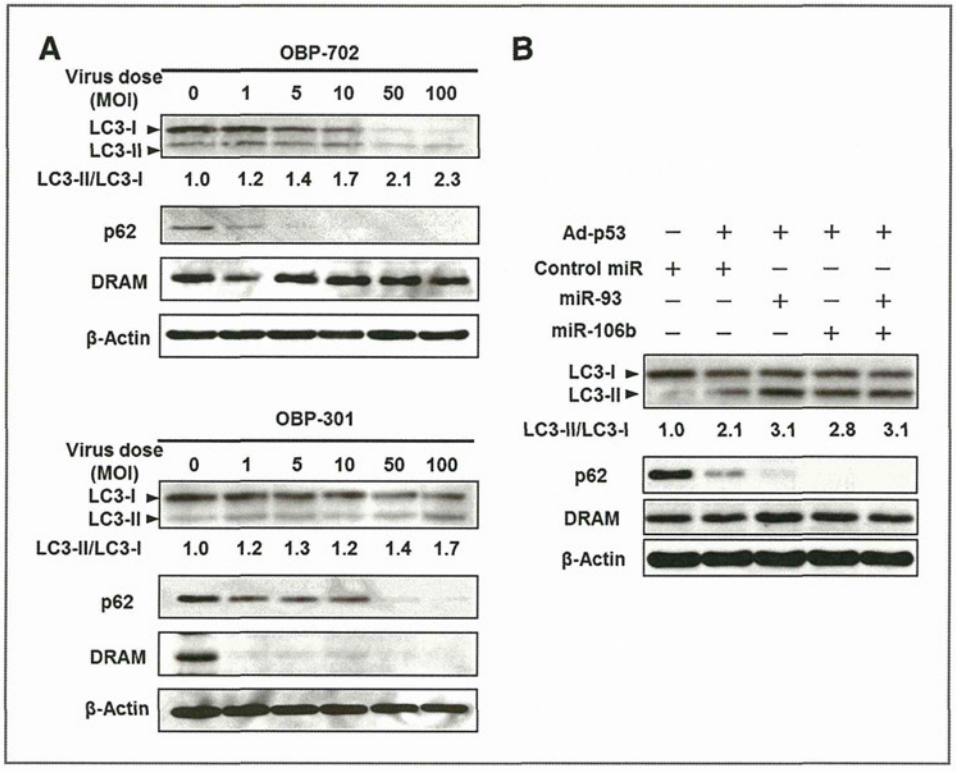


Figure 4. OBP-702 induces increased autophagy when compared with OBP-301. A, MNNG/HOS cells were infected with OBP-702 or OBP-301 at the indicated MOIs for 72 hours. Cell lysates were subjected to Western blot analysis for LC3, p62, and DRAM. B, SaOS-2 cells were transfected with 10 nmol/L *miR-93*, *miR-106*, or control miRNA 24 hours before Ad-p53 infection. At 48 hours after Ad-p53 infection at an MOI of 100, the expression levels of LC3, p62, and DRAM were examined by Western blot analysis. β-Actin was assayed as a loading control. By using ImageJ software, the ratio of LC3-II/LC3-I expressions was calculated relative to its expression in the mock-infected cells, whose expression level was designated as 1.0.

activity of oncolytic adenoviruses (34), the molecular mechanisms by which p53 mediates enhancement of the antitumor effect remain unclear. Recently, we reported that OBP-702 induces profound apoptosis through p53-dependent BAX upregulation and E1A-dependent p21 and MDM2 downregulation in epithelial malignant cells (26). Thus, oncolytic adenovirus-mediated p53 overexpression likely induces dual apoptotic and autophagic cell death pathways through p53-dependent BAX/DRAM activation and E1A-dependent p21/MDM2 suppression with E2F1-inducible *miR-93/106b* upregulation (Fig. 6).

OBP-702 efficiently suppressed the cell viability of both OBP-301–sensitive and -resistant osteosarcoma cells (Fig. 1). We previously reported that OBP-301–resistant SaOS-2 cells have no *hTERT* mRNA expression (Table 1), suggesting that SaOS-2 cells maintain telomere length through alternative lengthening of telomeres (ALT). As *hTERT* gene promoter is used for tumor-specific replication of OBP-301, ALT-type human osteosarcoma cells such as SaOS-2 cells may be resistant to OBP-301. However, ALT-type SaOS-2 cells showed similar sensitivity to OBP-702 as well as non–ALT-type MNNG/HOS cells (Fig. 1 and Table 1). These results suggest that p53 overexpression overcomes resistance to OBP-301 in ALT-type SaOS-2 cells. As the replication rate of OBP-702 was almost similar that of OBP-301 in ALT-type SaOS-2 cells (Supplementary Fig. S2), p53-induced cell death pathway would suppress the cell viability of ALT-type human osteosarcoma cells.

OBP-702–mediated p53 overexpression induced 2 types of programmed cell deaths (i.e., apoptosis and autophagy), thereby contributing to the enhancement of the antitumor effect of OBP-301 in human osteosarcoma cells (Fig. 2 and 4). As p53 downstream target p21 functions as a suppressor of apoptosis and autophagy (17, 18), p21 suppression may be a critical factor to induce dual programmed cell death pathways in response p53 overexpression. Suppression of p21 expression by genetic deletion or artificial p21 target microRNA has been shown to enhance the Ad-p53–induced apoptosis (18, 35). Inactivation of p21 by adenoviral E1A has been shown to enhance apoptosis in chemotherapeutic drug-treated human colon cancer cells that overexpress p53 (36). Genetic deletion of p21 has been also shown to induce autophagy in mouse embryonic fibroblasts treated with C (2)-ceramide or γ-irradiation (17). In contrast, p21 overexpression inhibited the Ad-p53–mediated apoptosis induction (18). Thus, E1A-mediated p21 downregulation would enhance p53-induced apoptosis and autophagy in OBP-702–infected cells.

E1A-dependent E2F1 activation and subsequent upregulation of E2F1-inducible miRNAs efficiently suppressed p21 expression, leading to the enhancement of p53-induced apoptosis and autophagy, in OBP-702–infected osteosarcoma cells (Figs. 2–4). Recent studies suggest that the cross-talk between p53 and E2F1 play a role in the regulation of diverse cell fates (37). For example, co-expression of p53 and E2F1 contributes to induction of apoptosis (38, 39). We previously showed

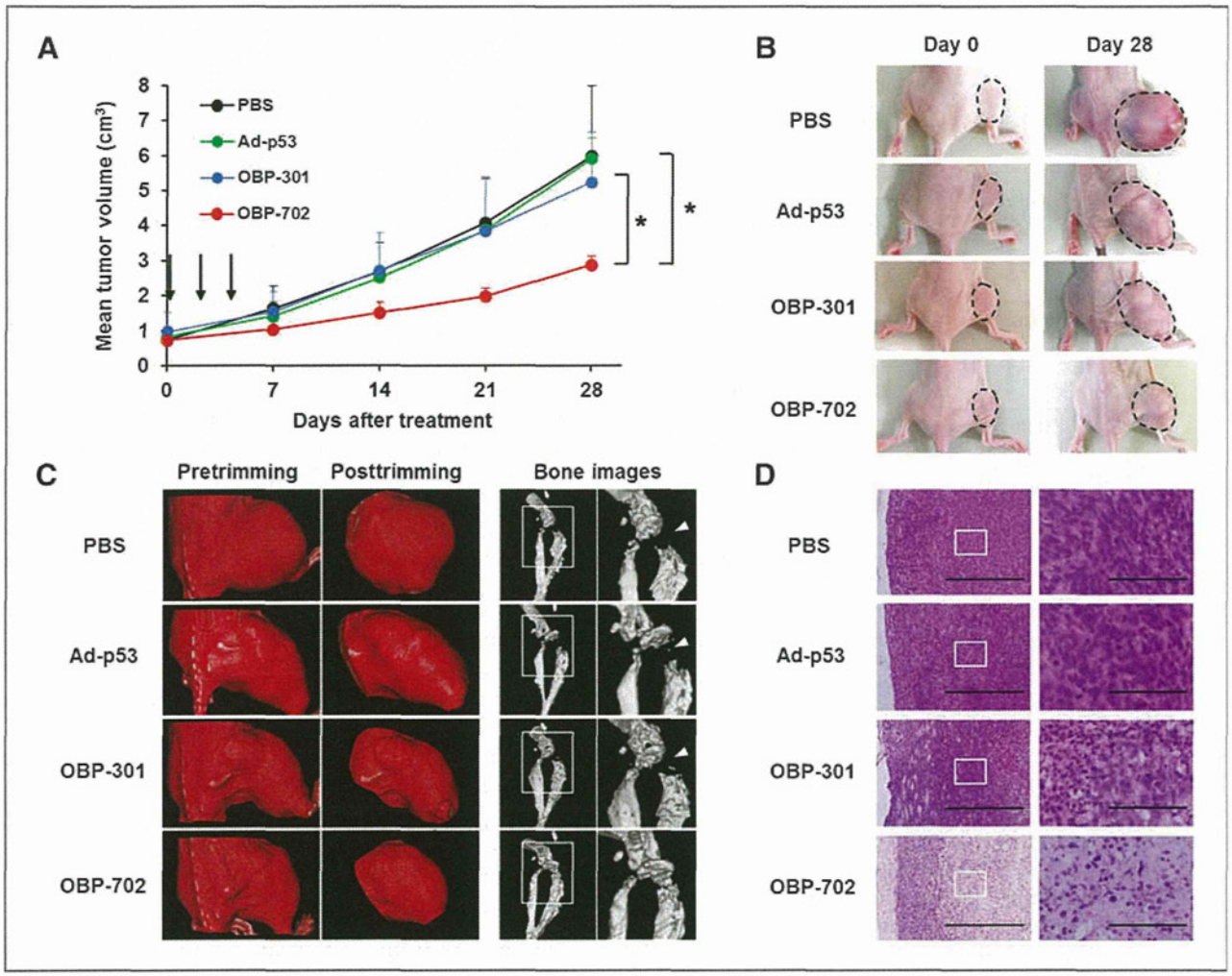


Figure 5. Antitumor effect of OBP-702 in an orthotopic MNNG/HOS osteosarcoma xenograft model. A, athymic nude mice were inoculated intratibially with MNNG/HOS cells ($5 \times 10^6$ cells/site). Twenty-one days after inoculation (designated as day 0), Ad-p53, OBP-301, or OBP-702 were injected into the tumor with $1 \times 10^8$ PFUs on days 0, 2, and 4 (black arrows). PBS was used as a control. Three mice were used for each group. Each tumor volume was assessed by CT examination. Tumor growth was expressed as mean tumor volume ± SD. Statistical significance was determined by Student *t* test. *, $P < 0.05$. B, macroscopic appearance of MNNG/HOS tumors in nude mice on days 0 and 28 after treatment with PBS, Ad-p53, OBP-301, or OBP-702. Tumor masses are outlined by a dotted line. C, 3D-CT images of MNNG/HOS tumors. The tumor volumes were calculated by the image viewer (INTAGE Realia) based on 3D-CT images of tumors after trimming. The white arrowheads indicate the osteolytic areas within tumor tissues treated with PBS, Ad-p53, or OBP-301. Left side images are low magnification and right side images are high magnification of the area outlined by a white square. D, histologic analysis of the MNNG/HOS tumors. Tumor tissues were obtained on day 28 after first treatment with PBS, Ad-p53, OBP-301, or OBP-702. Paraffin-embedded sections of MNNG/HOS tumors were stained with hematoxylin and eosin solutions. There were large necrotic areas in MNNG/HOS tumors treated with OBP-702. Left side images are low magnification and right side images are high magnification of the area outlined by a white square. Left scale bars, 500 μm. Right scale bars, 100 μm.

that E2F1 enhanced Ad-p53–mediated apoptosis through p14ARF-dependent MDM2 downregulation (39) and that OBP-702 infection showed E1A-dependent MDM2 downregulation in association with apoptosis (26). Recently, E2F1 has been shown to suppress MDM2 expression by suppressing the promoter activity (40) or by inducing upregulation of *miR-25/32*, which targets MDM2 (41). Furthermore, E2F1-inducible *miR-93/106b* enhanced Ad-p53–induced apoptosis and autophagy via p21 suppression (Figs. 3D and 4B). Therefore, the cooperation between the MDM2/p53/p21 pathway and the E2F1/miRNA pathway may be involved in the induction of apoptotic and autophagic cell death in response to OBP-702.

OBP-702–mediated p53 overexpression enhanced autophagy that was induced by oncolytic adenovirus in human osteosarcoma cells. OBP-702 infection induced increased expression of DRAM and decreased expression of p62 when compared with OBP-301 (Fig. 4), suggesting that OBP-702–mediated p53 overexpression enhances autophagy through DRAM activation. We recently reported that OBP-301 induces autophagy through E1A-dependent activation of E2F1/*miR-7* pathway and subsequent suppression of EGF receptor

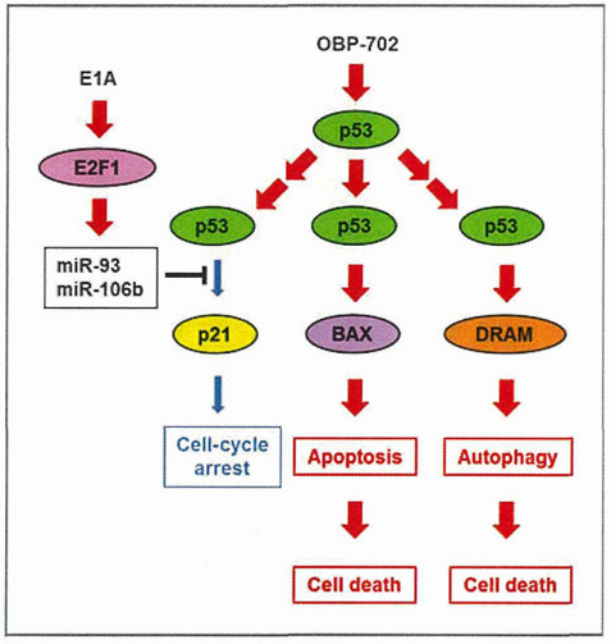


Figure 6. Outline of OBP-702–mediated induction of dual programmed cell death pathways. OBP-702 infection induces apoptosis and autophagy, leading to cell death, through p53-dependent BAX/DRAM upregulation and E1A-dependent p21 downregulation via E2F1-inducible *miR-93/106b* activation.

(EGFR; ref. 31). Restoration of p53 expression enhances the sensitivity to EGFR inhibitors in human cancer cells (42). Moreover, EGFR downregulation by transfection of specific antisense oligonucleotide promotes the differentiation status of human osteosarcoma U2OS cells (43). Thus, OBP-702 may induce differentiation as well as cell death through autophagy activation by DRAM upregulation and EGFR downregulation in human osteosarcoma cells.

The 3D-CT imaging system was a useful method to assess both tumor volume and bone destruction status in MNNG/HOS tumors. OBP-702–treated tumors were smaller and had less bone destruction than PBS-, Ad-p53-, or OBP-301–treated tumors (Fig. 5A and C). Recent reports have suggested that zoledronic acid suppresses tumor growth as well as osteolytic components in human osteosarcoma xenograft tumor models (44, 45). These results suggest that combination therapy with OBP-702 and zoledronic acid may be more effective and more protective against bone destruction in human osteosarcomas. Further study using a 3D-CT imaging system may provide important information about bone destruction status in osteosarcomas treated with OBP-702 and zoledronic acid.

Adenovirus-mediated *p53* gene therapy exerts an antitumor effect in human osteosarcoma cells (46). However, the antitumor activity of replication-deficient Ad-p53 is limited in some human osteosarcoma cells (47). Ad-p53–mediated p53 overexpression increases the sensitivity of human osteosarcoma cells to the chemotherapeutic drugs, cisplatin and doxorubicin (48). A synergistic antitumor effect between doxorubicin and roscovitine was also associated with autophagy induction in human osteosarcoma U2OS cells (49). As OBP-702 induced more profound apoptosis and autophagy than did OBP-301 or Ad-p53 (Fig. 2 and 4), combination therapy with OBP-702 and chemotherapeutic agents may be more effective than monotherapy with OBP-702. Moreover, a recent report has shown that p53-armed replication-competent oncolytic adenovirus is a safe antitumor agent in rodents and non-human primates (50). However, for clinical application of OBP-702, it must be necessary to establish the systemic delivery method and confirm the host biologic contributions in patients with cancer. Although there are some unsolved issues, the combination of p53-armed oncolytic adenovirus and chemotherapy may provide us a promising antitumor strategy against human osteosarcoma cells.

In conclusion, we clearly showed that the p53-expressing oncolytic adenovirus OBP-702 has a much stronger antitumor effect than does OBP-301. Oncolytic adenovirus-mediated *p53* gene transduction may induce dual apoptotic and autophagic cell death pathways through p53-dependent activation of cell death inducers and E1A-dependent suppression of cell death inhibitors, resulting in the enhancement of antitumor effect.

## Disclosure of Potential Conflicts of Interest

Y. Urata is President & CEO of Oncolys BioPharma, Inc., the manufacturer of OBP-301 (Telomelysin). H. Tazawa and T. Fujiwara are consultants of Oncolys BioPharma, Inc. No potential conflicts of interest were disclosed by the other authors.

## Authors' Contributions

**Conception and design:** J. Hasei, F. Uno, S. Kagawa, T. Ozaki, T. Fujiwara
**Development of methodology:** J. Hasei, F. Uno, S. Kagawa
**Acquisition of data (provided animals, acquired and managed patients, provided facilities, etc.):** J. Hasei, H. Tazawa, S. Osaki, Y. Yamakawa, A. Yoshida, T. Onishi, T. Ozaki
**Analysis and interpretation of data (e.g., statistical analysis, biostatistics, computational analysis):** J. Hasei, H. Tazawa, T. Fujiwara
**Writing, review, and/or revision of the manuscript:** J. Hasei, H. Tazawa, T. Kunisada, Y. Urata, T. Fujiwara
**Administrative, technical, or material support (i.e., reporting or organizing data, constructing databases):** H. Tazawa, T. Kunisada, Y. Hashimoto, S. Kagawa, Y. Urata, T. Ozaki
**Study supervision:** T. Sasaki, T. Kunisada, F. Uno, Y. Urata, T. Fujiwara

## Acknowledgments

The authors thank Dr. Satoru Kyo (Kanazawa University) for providing the HOS and SaOS-2 cells and Tomoko Sueishi for her excellent technical support.

## Grant Support

This study was supported by grants-in-aid from the Ministry of Education, Science, and Culture, Japan (T. Fujiwara) and grants from the Ministry of Health and Welfare, Japan (T. Fujiwara), and in part by the National Cancer Center Research and Development Fund (23-A-10) (T. Ozaki).

The costs of publication of this article were defrayed in part by the payment of page charges. This article must therefore be hereby marked *advertisement* in accordance with 18 U.S.C. Section 1734 solely to indicate this fact.

Received August 30, 2012; revised December 27, 2012; accepted December 29, 2012; published OnlineFirst January 11, 2013.

## References


1. Ottaviani G, Jaffe N. The etiology of osteosarcoma. Cancer Treat Res 2009;152:15–32.
2. Damron TA, Ward WG, Stewart A. Osteosarcoma, chondrosarcoma, and Ewing's sarcoma: National Cancer Data Base Report. Clin Orthop Relat Res 2007;459:40–7.
3. Lewis IJ, Nooij MA, Whelan J, Sydes MR, Grimer R, Hogendoorn PC, et al. Improvement in histologic response but not survival in osteosarcoma patients treated with intensified chemotherapy: a randomized phase III trial of the European Osteosarcoma Intergroup. J Natl Cancer Inst 2007;99:112–28.
4. Bacci G, Longhi A, Versari M, Mercuri M, Briccoli A, Picci P. Prognostic factors for osteosarcoma of the extremity treated with neoadjuvant chemotherapy: 15-year experience in 789 patients treated at a single institution. Cancer 2006;106:1154–61.
5. Bielack SS, Kempf-Bielack B, Delling G, Exner GU, Flege S, Helmke K, et al. Prognostic factors in high-grade osteosarcoma of the extremities or trunk: an analysis of 1,702 patients treated on neoadjuvant cooperative osteosarcoma study group protocols. J Clin Oncol 2002; 20:776–90.
6. Siegel R, Naishadham D, Jemal A. Cancer statistics, 2012. CA Cancer J Clin 2012;62:10–29.
7. Buseman CM, Wright WE, Shay JW. Is telomerase a viable target in cancer? Mutat Res 2012;730:90–7.
8. Artandi SE, DePinho RA. Telomeres and telomerase in cancer. Carcinogenesis 2010;31:9–18.
9. Umehara N, Ozaki T, Sugihara S, Kunisada T, Morimoto Y, Kawai A, et al. Influence of telomerase activity on bone and soft tissue tumors. J Cancer Res Clin Oncol 2004;130:411–6.
10. Aogi K, Woodman A, Urquidi V, Mangham DC, Tarin D, Goodison S. Telomerase activity in soft-tissue and bone sarcomas. Clin Cancer Res 2000;6:4776–81.
11. Nakayama J, Tahara H, Tahara E, Saito M, Ito K, Nakamura H, et al. Telomerase activation by hTRT in human normal fibroblasts and hepatocellular carcinomas. Nat Genet 1998;18:65–8.
12. Kawashima T, Kagawa S, Kobayashi N, Shirakiya Y, Umeoka T, Teraishi F, et al. Telomerase-specific replication-selective virotherapy for human cancer. Clin Cancer Res 2004;10:285–92.
13. Nemunaitis J, Tong AW, Nemunaitis M, Senzer N, Phadke AP, Bedell C, et al. A phase I study of telomerase-specific replication competent oncolytic adenovirus (telomelysin) for various solid tumors. Mol Ther 2010;18:429–34.
14. Sasaki T, Tazawa H, Hasei J, Kunisada T, Yoshida A, Hashimoto Y, et al. Preclinical evaluation of telomerase-specific oncolytic virotherapy for human bone and soft tissue sarcomas. Clin Cancer Res 2011;17:1828–38.
15. Li G, Kawashima H, Ogose A, Ariizumi T, Xu Y, Hotta T, et al. Efficient virotherapy for osteosarcoma by telomerase-specific oncolytic adenovirus. J Cancer Res Clin Oncol 2011;137:1037–51.
16. Vousden KH, Prives C. Blinded by the light: the growing complexity of p53. Cell 2009;137:413–31.
17. Fujiwara K, Daido S, Yamamoto A, Kobayashi R, Yokoyama T, Aoki H, et al. Pivotal role of the cyclin-dependent kinase inhibitor p21WAF1/CIP1 in apoptosis and autophagy. J Biol Chem 2008;283:388–97.
18. Gorospe M, Cirielli C, Wang X, Seth P, Capogrossi MC, Holbrook NJ. p21(Waf1/Cip1) protects against p53-mediated apoptosis of human melanoma cells. Oncogene 1997;14:929–35.
19. Blagosklonny MV, el-Deiry WS. In vitro evaluation of a p53-expressing adenovirus as an anti-cancer drug. Int J Cancer 1996;67:386–92.
20. Zeng Y, Prabhu N, Meng R, Eldeiry W. Adenovirus-mediated p53 gene therapy in nasopharyngeal cancer. Int J Oncol 1997;11:221–6.
21. Clayman GL, el-Naggar AK, Lippman SM, Henderson YC, Frederick M, Merritt JA, et al. Adenovirus-mediated p53 gene transfer in patients with advanced recurrent head and neck squamous cell carcinoma. J Clin Oncol 1998;16:2221–32.
22. Swisher SG, Roth JA, Nemunaitis J, Lawrence DD, Kemp BL, Carrasco CH, et al. Adenovirus-mediated p53 gene transfer in advanced non-small-cell lung cancer. J Natl Cancer Inst 1999;91:763–71.
23. Shimada H, Matsubara H, Shiratori T, Shimizu T, Miyazaki S, Okazumi S, et al. Phase I/II adenoviral p53 gene therapy for chemoradiation resistant advanced esophageal squamous cell carcinoma. Cancer Sci 2006;97:554–61.
24. Fujiwara T, Tanaka N, Kanazawa S, Ohtani S, Saijo Y, Nukiwa T, et al. Multicenter phase I study of repeated intratumoral delivery of adenoviral p53 in patients with advanced non-small-cell lung cancer. J Clin Oncol 2006;24:1689–99.
25. Sakai R, Kagawa S, Yamasaki Y, Kojima T, Uno F, Hashimoto Y, et al. Preclinical evaluation of differentially targeting dual virotherapy for human solid cancer. Mol Cancer Ther 2010;9:1884–93.
26. Yamasaki Y, Tazawa H, Hashimoto Y, Kojima T, Kuroda S, Yano S, et al. A novel apoptotic mechanism of genetically engineered adenovirus-mediated tumour-specific p53 overexpression through E1A-dependent p21 and MDM2 suppression. Eur J Cancer 2012;48: 2282–91.
27. Hashimoto Y, Watanabe Y, Shirakiya Y, Uno F, Kagawa S, Kawamura H, et al. Establishment of biological and pharmacokinetic assays of telomerase-specific replication-selective adenovirus. Cancer Sci 2008;99:385–90.
28. Bagchi S, Raychaudhuri P, Nevins JR. Adenovirus E1A proteins can dissociate heteromeric complexes involving the E2F transcription factor: a novel mechanism for E1A trans-activation. Cell 1990;62: 659–69.
29. Emmrich S, Putzer BM. Checks and balances: E2F-microRNA crosstalk in cancer control. Cell Cycle 2010;9:2555–67.
30. Petrocca F, Vecchione A, Croce CM. Emerging role of miR-106b-25/miR-17-92 clusters in the control of transforming growth factor beta signaling. Cancer Res 2008;68:8191–4.
31. Tazawa H, Yano S, Yoshida R, Yamasaki Y, Sasaki T, Hashimoto Y, et al. Genetically engineered oncolytic adenovirus induces autophagic cell death through an E2F1-microRNA-7-epidermal growth factor receptor axis. Int J Cancer 2012;131:2939–50.
32. Crighton D, Wilkinson S, O'Prey J, Syed N, Smith P, Harrison PR, et al. DRAM, a p53-induced modulator of autophagy, is critical for apoptosis. Cell 2006;126:121–34.
33. Liu TC, Galanis E, Kirn D. Clinical trial results with oncolytic virotherapy: a century of promise, a decade of progress. Nat Clin Pract Oncol 2007;4:101–17.
34. van Beusechem VW, van den Doel PB, Grill J, Pinedo HM, Gerritsen WR. Conditionally replicative adenovirus expressing p53 exhibits enhanced oncolytic potency. Cancer Res 2002;62:6165–71.
35. Idogawa M, Sasaki Y, Suzuki H, Mita H, Imai K, Shinomura Y, et al. A single recombinant adenovirus expressing p53 and p21-targeting artificial microRNAs efficiently induces apoptosis in human cancer cells. Clin Cancer Res 2009;15:3725–32.
36. Chattopadhyay D, Ghosh MK, Mal A, Harter ML. Inactivation of p21 by E1A leads to the induction of apoptosis in DNA-damaged cells. J Virol 2001;75:9844–56.
37. Polager S, Ginsberg D. p53 and E2f: partners in life and death. Nat Rev Cancer 2009;9:738–48.
38. Wu X, Levine AJ. p53 and E2F-1 cooperate to mediate apoptosis. Proc Natl Acad Sci U S A 1994;91:3602–6.
39. Itoshima T, Fujiwara T, Waku T, Shao J, Kataoka M, Yarbrough WG, et al. Induction of apoptosis in human esophageal cancer cells by sequential transfer of the wild-type p53 and E2F-1 genes: involvement of p53 accumulation via ARF-mediated MDM2 down-regulation. Clin Cancer Res 2000;6:2851–9.
40. Tian X, Chen Y, Hu W, Wu M. E2F1 inhibits MDM2 expression in a p53-dependent manner. Cell Signal 2011;23:193–200.
41. Suh SS, Yoo JY, Nuovo GJ, Jeon YJ, Kim S, Lee TJ, et al. MicroRNAs/TP53 feedback circuitry in glioblastoma multiforme. Proc Natl Acad Sci U S A 2012;109:5316–21.
42. Huang S, Benavente S, Armstrong EA, Li C, Wheeler DL, Harari PM. p53 modulates acquired resistance to EGFR inhibitors and radiation. Cancer Res 2011;71:7071–9.
43. Salvatori L, Caporuscio F, Coroniti G, Starace G, Frati L, Russo MA, et al. Down-regulation of epidermal growth factor receptor induced by estrogens and phytoestrogens promotes the differentiation of U2OS human osteosarcoma cells. J Cell Physiol 2009;220: 35–44.

44. Dass CR, Choong PF. Zoledronic acid inhibits osteosarcoma growth in an orthotopic model. Mol Cancer Ther 2007;6:3263–70.
45. Labrinidis A, Hay S, Liapis V, Ponomarev V, Findlay DM, Evdokiou A. Zoledronic acid inhibits both the osteolytic and osteoblastic components of osteosarcoma lesions in a mouse model. Clin Cancer Res 2009;15:3451–61.
46. Ternovoi VV, Curiel DT, Smith BF, Siegal GP. Adenovirus-mediated p53 tumor suppressor gene therapy of osteosarcoma. Lab Invest 2006;86:748–66.
47. Hellwinkel OJ, Muller J, Pollmann A, Kabisch H. Osteosarcoma cell lines display variable individual reactions on wildtype p53 and Rb tumour-suppressor transgenes. J Gene Med 2005;7:407–19.
48. Ganjavi H, Gee M, Narendran A, Parkinson N, Krishnamoorthy M, Freedman MH, et al. Adenovirus-mediated p53 gene therapy in osteosarcoma cell lines: sensitization to cisplatin and doxorubicin. Cancer Gene Ther 2006;13:415–9.
49. Lambert LA, Qiao N, Hunt KK, Lambert DH, Mills GB, Meijer L, et al. Autophagy: a novel mechanism of synergistic cytotoxicity between doxorubicin and roscovitine in a sarcoma model. Cancer Res 2008;68:7966–74.
50. Su C, Cao H, Tan S, Huang Y, Jia X, Jiang L, et al. Toxicology profiles of a novel p53-armed replication-competent oncolytic adenovirus in rodents, felids, and nonhuman primates. Toxicol Sci 2008;106:242–50.

IJC
International Journal of Cancer

# A novel synergistic effect of iron depletion on antiangiogenic cancer therapy

Toshiaki Ohara[1], Kazuhiro Noma[1], Shinichi Urano[1], Shinichiro Watanabe[1], Seishi Nishitani[1], Yasuko Tomono[2], Fumiaki Kimura[3], Shunsuke Kagawa[1], Yasuhiro Shirakawa[1] and Toshiyoshi Fujiwara[1]

[1] Department of Gastroenterological Surgery, Okayama University Graduate School of Medicine, Dentistry and Pharmaceutical Sciences, Okayama, Japan
[2] Shigei Medical Research Institute, Okayama, Japan
[3] Department of Internal Medicine, Tamano City Hospital, Okayama, Japan

**Iron is an essential element for both normal and cancer cells in humans. Treatment to reduce iron levels has been shown to suppress tumor growth *in vivo*. However, iron depletion monotherapy by iron decreased treatment has not been thought to be superior to ordinary chemotherapy and is not part of the standard therapeutic strategy for the treatment of cancer. Iron depletion is also known to reduce serum hemoglobin and oxygen supply to the tissue, which indicates that iron depletion may induce angiogenesis. Therefore, we hypothesized that iron depletion with antiangiogenic therapy can have a novel therapeutic effect in the treatment of cancer. Human nonsmall cell carcinoma cell lines A549 and H1299 were used in our study. An iron-deficient diet and an iron chelator were used to simulate an iron-depleted condition. The antitumor effects of iron depletion and antiangiogenic therapy were determined on A549 xenograft mice. The iron-depleted condition produced by an iron-deficient diet suppressed tumor growth. Tumor tissue from the iron-deficient diet group showed that cancer cell proliferation was suppressed and hypoxia was induced. Microvessel density of this group was increased which suggested that the iron-depleted condition induced angiogenesis. Bevacizumab administration had a synergetic effect on inhibiting the tumor growth on Day 39. An iron-depleted condition inhibited cancer cell proliferation and reciprocally induced angiogenesis. Bevacizumab synergistically enhanced the iron-depleted antitumor effect. Treatment to deplete iron levels combined with anti-angiogenic therapy could induce a novel therapeutic effect in the treatment of cancer.**

## Introduction

Chemotherapy is continually evolving and various anticancer drugs have been produced during the past decades. Recently, therapies targeting molecules in cancer cells have been developed and used in the clinical setting. Moreover, new drugs targeting the tumor stroma have been developed. Bevacizumab, an antibody against vascular endothelial growth factor (VEGF), is the first tumor stroma molecular-targeting drug.[1] Many kinds of cancer cells are known to become hypoxic during progression of the tumor. However, the cells survive with angiogenesis through activation of VEGF signaling *via* hypoxia-induced factor 1α (HIF-1α).[2] Bevacizumab has been used to treat many different cancers all over the world and some clinical studies revealed that bevacizumab prolonged survival.[3–5]

Iron metabolism and its relationship with cancer cells have been studied for a long time. Iron is an essential element for both human normal and cancer cells. Iron overload is known to induce some kinds of cancer, which suggests that the prevention of iron overload may become a therapeutic strategy for cancer prevention.[6,7] In fact, reduction of serum iron with phlebotomy lowered the risk of developing hepatocellular carcinoma in patients with chronic hepatitis C.[8] Iron-depletion treatment is also known to suppress tumor growth *in vivo*.[9] However, iron-depletion monotherapy has generally been thought to not be superior to ordinary chemotherapy and a standard therapeutic strategy in the treatment of cancer.

In human biology, iron depletion was known to reduce serum hemoglobin and oxygen supply to the tissue.[10,11] Therefore, cancer cells could respond to iron depletion and induce angiogenesis to compensate for the reduced oxygen supply. Subsequently, their iron-decreased status could make the cancer cell more dependent on angiogenesis so that the effectiveness of antiangiogenic therapy would be increased in an iron-depleted condition.

**Key words:** angiogenesis, bevacizumab, chelator, iron

**Abbreviations**: CD31: cluster of differentiation 31; HIF-1α: hypoxia-induced factor 1α; MVD: microvessel density; NSCLC: non-small cell lung cancer; RECIST: response evaluation criteria in solid tumors; TfR-1: transferrin receptor 1; VEGF: vascular endothelial factor

Additional Supporting Information may be found in the online version of this article.

**Grant sponsors:** Grants-in-Aid from the Ministry of Education, Science, and Culture, Japan, The Ministry of Health and Welfare, Japan

**DOI:** 10.1002/ijc.27943

**History:** Received 15 Jun 2012; Accepted 17 Oct 2012; Online 15 Nov 2012

**Correspondence to:** Toshiyoshi Fujiwara, Department of Gastroenterological Surgery, Okayama University Graduate School of Medicine, Dentistry and Pharmaceutical Sciences, 2-5-1 Shikata-cho, Kita-ku, Okayama 700-8558, Japan, Tel: +81-86-235-7257, Fax: +81-86-221-8775, E-mail: toshi_f@md.okayama-u.ac.jp

**What's new?**
**Withholding iron from tissues reduces their access to oxygen, and can suppress tumor cell proliferation. If reducing the availability of iron could weaken tumors, making them less able to withstand traditional therapies, that would be an inexpensive and simple way to boost outcomes. The current study investigated whether limiting the iron supply enhanced the effectiveness of anti-angiogenic therapy. In mice fed an iron-deficient diet, tumor growth slowed. When an iron-chelating agent was used in conjunction with the anti-angiogenesis drug bevacizumab, the anti-tumor treatment worked significantly better, suggesting that iron reduction could be a very promising way to enhance cancer therapy.**

In our study, we investigated whether iron-depletion and anti-angiogenic therapy can have a novel therapeutic effect for the treatment of cancer.

## Material and Methods

### Cell lines and cultures

The human nonsmall cell lung cancer (NSCLC) cell lines A549 and H1299 were used in our study. A549 was cultured in Dulbecco's modified eagle medium (DMEM, Sigma-Aldrich, St. Louis, MO) and H1299 was cultured in RPMI1640 medium (Sigma-Aldrich) at 37°C in humidified air with 5% $CO_2$. Each medium was supplemented with 10% fetal calf serum (FCS, Hyclone, Logan, UT), 100 units/mL penicillin, and 100 mg/mL streptomycin (Sigma-Aldrich).

### Reagents

Bevacizumab, commercialized as AVASTIN™ by Roche (Basel, Switzerland), was purchased from Chugai Pharmaceutical (Tokyo, Japan). Bevacizumab was diluted to the final concentration of 5 mg/kg with 0.9% sodium chloride before use *in vivo*. Deferasirox, commercialized as EXJADE™ was purchased from Novartis Pharma (Tokyo, Japan).

### Cell viability assay

The proliferation of A549 and H1299 cells was evaluated using a sulfonated tetrazolium salt (WST-1). The cells were plated at a density of $1 \times 10^3$ cells/well in 96-well micro plates, in 10% FCS containing each mediu, and incubated at 37°C in a humidified atmosphere of 5% $CO_2$. Twenty-four hours after each treatment, the cells were incubated with 10 μL/well of WST-1/PBS solution (Roche) for 3 hr under the same conditions as indicated above. The absorbance of the samples was measured at 450 nm using a microplate reader with a background control as the blank. The cell viability ratio was expressed as a percentage of the control.

### Cell-cycle analysis by flow cytometry

For the cell-cycle analysis, cancer cells were plated in six-well tissue culture plates and treated with different concentrations of deferasirox (0, 1, 10,100 or 1,000 μM). After 24 hr, the cells were harvested and stained with 20 mg/mL propidium iodide. The DNA content was analyzed with a fluorescence-activated cell sorter (FACScan, Becton Dickinson, Franklin Lakes, NJ) using Cell Quest software (BD Biosciences, San Jose, CA).

### Western blotting

Whole-cell lysates and nuclear protein were extracted using M-PER buffer (Thermo Fisher Scientific, Rockford, IL) and NE-PER buffer (Thermo Fisher Scientific), respectively. Total protein extraction and nuclear protein from homogenized A549 xenograft tumor tissue samples were extracted using T-PER buffer (Thermo Fisher Scientific) and NE-PER buffer (Thermo Fisher Scientific). The collected supernatants were subjected to protein concentration and equal amounts of protein were electrophoresed under reducing conditions in gradient polyacrylamide gels (ATTO, Tokyo, Japan) and were then transferred onto polyvinylidene difluoride filter membranes (Millipore, Billerica, MA). The membranes were incubated with primary antibodies at 4°C overnight, followed by incubation with secondary antibodies at room temperature for 1 hr. An Amersham chemiluminescent ECL Plus Western Blotting Detection system (GE Healthcare, Piscataway, NJ) was used for signal detection. Western blotting materials were as follows: hydroxy-HIF-1α (Pro564) (D43B5) was obtained from Cell Signaling Technology (Beverly, MA); cyclin D1 was obtained from Santa Cruz Biotechnology (Santa Cruz, CA); β-actin was obtained from Sigma-Aldrich; horseradish peroxidase-conjugated rabbit anti-mouse IgG was obtained from Dako Cytomation (Glostrup, Denmark); and goat anti-rabbit IgG was obtained from American Qualex Antibodies (La Mirada, CA).

### Histology and immunohistology

Surgically resected tissues from the A549 xenograft model were used for histological and immunohistochemical study. Paraffin sections were prepared from the 10% formalin-fixed tumors and stained with hematoxylin/eosin and Prussian blue. Prussian blue staining was performed by incubating fixed tissue in a mixture of 2% potassium ferrocyanide and 1% HCl for 30 min. Glass slides were rinsed in distilled water and counterstained with Nuclear Fast Red for 5 min. Immunohistochemical procedures were followed as described previously.[12] Deparaffinized tissue sections were immersed in methanol containing 3% hydrogen peroxide to block endogenous peroxide activity. An autoclave pretreatment in citrate buffer was done for antigen retrieval. A Ki-67 staining kit (Dako) and CD31 (endothelial cell adhesion molecule-1) rabbit monoclonal antibody (Santa Cruz Biotechnology) were used. After incubation with a blocking buffer, the sections were treated with Ki-67 and CD31 antibodies for 1 hr at room temperature followed by immunobridging with Avidin DH-biotinylated

**Table 1.** Content of control and iron-deficient diets

| | Control diet | Iron-deficient diet |
|---|---|---|
| **g/kg diet** | | |
| Corn starch | 610 | 610 |
| Casein | 220 | 220 |
| Cellulose | 50 | 50 |
| Soybean oil | 40 | 40 |
| Vitamin mixture | 10 | 10 |
| *Mineral mixture* | | |
| Potassium | 17.3 | 17.3 |
| Phosphorus | 15 | 15 |
| Calcium | 13.55 | 13.55 |
| Magnesium | 8 | 8 |
| Corn starch | 8 | 9.9 |
| Sodium | 6 | 6 |
| Iron | 1.9 | |
| Manganese | 0.154 | 0.154 |
| Zinc | 0.06 | 0.06 |
| Iodine | 0.0154 | 0.0154 |
| Copper | 0.0126 | 0.0126 |
| Chloride | 0.004 | 0.004 |

horseradish peroxide complex (Nichirei, Tokyo, Japan). Signal detection was done for 2–5 min using a solution of 3,3′-diaminobenzidine tetrahydrochloride in 50 mmol/L Tris-HCl (pH = 7.5) containing 0.001% hydrogen peroxide. The sections were counterstained with Mayer's hematoxylin for 6 hr at room temperature followed by immunobridging with Avidin DH-biotinylated horseradish peroxide complex (Nichirei). Ki-67 labeling index was calculated as the average percentage of Ki-67-positive nuclei in three high-power fields (HPFs).

### Hypoxia assay

A Hypoxyprobe-1 kit (Chemicon International, Temecula, CA) was used to investigate tumor hypoxia. Mice were injected intraperitoneally (ip) with Hypoxyprobe TM-1 [pimonidazole hydrochloride 60 mg/kg] 45 min before tumor collection.[13,14] The collected tumor sections were incubated for 1 h with the Hypoxyprobe-1 primary antibody supplied with the kit.

### Micro vessel density

Angiogenesis activity was determined to count microvessel density. CD31-immunostained sections were used in the previous report.[15] The highest density of blood vessels (hot spots) was selected at a low-power field and the number of blood vessels was counted per 0.20 $mm^2$ in five separate hot spots at a HPF.[16] All sections were scored independently by two individual experienced microscopists and no significant differences were observed between scorers.

**Table 2.** Blood analysis results of the normal and iron-deficient diet groups

| | Fe (+) | Fe (−) | *p*-Value |
|---|---|---|---|
| RBC ($\times 10^4$) | 891 ± 46 | 802 ± 43 | 0.029 |
| WBC | 4,425 ± 1,258 | 3,575 ± 150 | 0.228 |
| Hb | 14.9 ± 0.7 | 11.4 ± 0.6 | 0.001 |
| HCT | 46.2 ± 3.7 | 38.5 ± 3.8 | 0.027 |
| MCV | 52.0 ± 2.0 | 48.5 ± 2.4 | 0.065 |
| MCHC | 30.3 ± 1.3 | 29.8 ± 1.3 | 0.594 |
| Fe | 222.3 ± 20.1 | 115.3 ± 43.3 | 0.004 |
| Ferritin | 255.0 ± 108.6 | 113.8 ± 24.9 | 0.044 |

### VEGF ELISA assay

To evaluate the supernatant VEGF secreted by A549 and H1299 cells, we used a VEGF enzyme-linked immunosorbent assay (ELISA) kit (R&D Systems, Minneapolis, MN). The cancer cells were plated in six-well tissue culture plates and were treated with different concentrations of deferasirox (0, 1, 10, 100 or 1,000 μM). After a 24-hr treatment, the supernatant and cells were harvested and VEGF content was assayed by ELISA according to the protocol provided by the manufacturer. The results were normalized to the concentration of total protein extraction per plate. Data were presented as mean ± SD from three independent experiments.

### Animal experiments

The animal experimental protocol was approved by the Ethics Review Committee for Animal Experimentation of Okayama University, Okayama, Japan. All of the mice and their diets (normal and iron deficient) were purchased from Clea (Tokyo, Japan) (Table 1). The 6-week-old male BALB/c nu/nu mice were randomized into two groups of eight mice each; (*i*) normal diet as a control and (*ii*) iron-deficient diet. After 3 weeks, A549 subcutaneous xenografts were produced on the backs of mice by injecting $3 \times 10^6$ cells mixed with Matrigel (BD Biosciences) at a 1:1 ratio.[17,18] Water was provided and the mice were allowed to drink freely. Tumor volume was measured weekly (length × width$^2$/2). For the bevacizumab administration study, 6-week-old male BALB/c nu/nu mice were randomized into two groups of 20 mice each as above. After 3 weeks, A549 subcutaneous xenografts were produced in the same way. After a week, the mice in each diet group were randomized into two groups of four mice each (*i*) bevacizumab (5 mg/kg twice/week for 5 weeks), (*ii*) saline alone as a control.[15] The drug was administered ip and tumor volume measured twice a week. Both diets (normal and iron deficient) and water were provided *ad libitum*.

### Statistical analysis

A Student's *t*-test was used to compare data between the two groups. Data represent the mean ± SD; $p < 0.05$ was considered statistically significant.

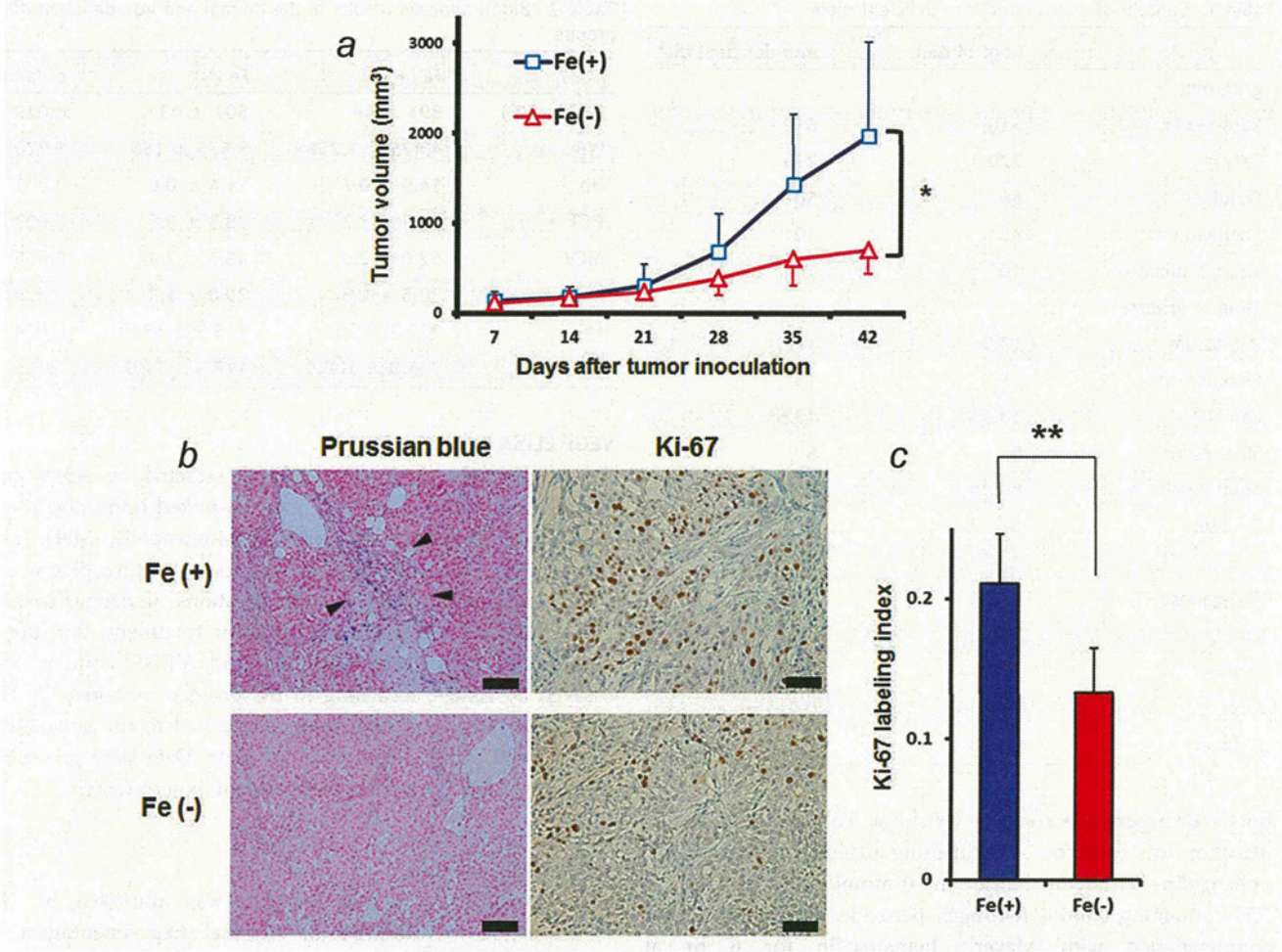


**Figure 1.** Iron depletion suppressed tumor growth *in vivo*. (*a*) An iron-deficient diet was started 3 weeks before inoculating A549 cells on the backs of mice. The iron-deficient diet was continuously fed until the end of the study. Tumor volume was measured as a cube (length × width × height) and was tracked up to 6 weeks. Tumor growth was suppressed in the iron-deficient diet group. Tumor growth was expressed as mean tumor volume ± SD. Statistical significance (*) was determined as $p < 0.01$. (*b*) Prussian blue and Ki-67 staining showed the positive spot area and proliferating cells were reduced in the iron-depleted condition. Scale bars: 50 mm. (*c*) Ki-67 labeling index was decreased in iron-depleted condition. Data are means ± SD. Statistical significance (**) was determined as $p < 0.05$.

## Results

### Iron-deficient diet produced iron-depleted mice

We first confirmed that the iron-deficient diet resulted in an iron-depleted mouse model. The 6-week-old male BALB/c nu/nu mice were randomized into two groups of eight mice each. Blood sampling was performed after 3 weeks. The iron-deficient diet reduced serum iron levels (Table 2). To confirm iron deficiency histologically, Prussian blue staining was done using surgically resected murine spleens. Although the positive blue spots were diffusely recognized in the normal diet group, no positive blue spot was recognized in the iron-deficient diet group (Supporting Information Fig. 1). A reduction of iron in the reticuloendothelial system proves that the iron-deficient diet reduced serum iron levels.

### Iron depletion suppressed tumor growth

We investigated the tumor growth under an iron-depleted condition. A549 subcutaneous xenografts were produced on the backs of mice after 3 weeks of an iron-deficient diet and tumor size was measured once a week. Tumor growth was suppressed in the iron-deficient diet group (tumor volume: normal diet *vs.* iron-deficient diet = 1,375.9 ± 688.4 *vs.* 497.0 ± 192.2 $mm^3$; $p = 0.0037$) (Fig. 1*a*). There were no mice that died and no significant side effects were observed during the experiment. Moreover, diet intake and body weight were not significantly different between normal diet group and iron-deficient diet group (Supporting Information Fig. S2).

Iron depletion reduced iron levels in tumor tissue and suppressed cancer cell proliferation

To identify the differences in tumor progression in an iron-depleted condition, we performed histological and immunohistological examinations (Fig. 1*b*). As shown above, an iron-deficient diet reduced the serum and tumor tissue iron levels. Interestingly, there was only difference of positive spot area in stroma tissue of the tumor. Proliferating cells (G1, S, G2 and M cycling stages of cell division) were stained

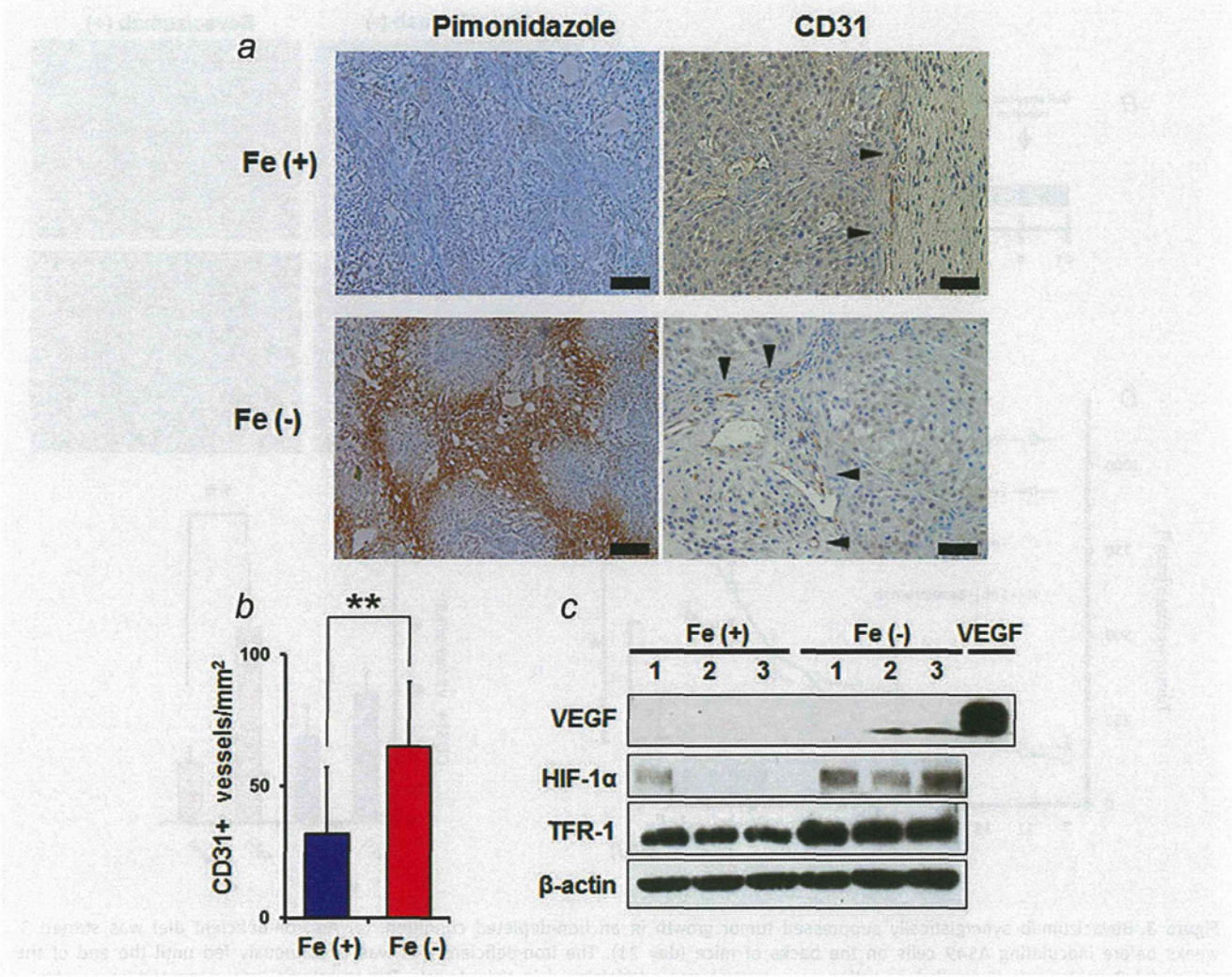


**Figure 2.** Iron depletion reciprocally induced angiogenesis *via* upregulation of HIF-1α. (*a*) Tumor tissues obtained as described in the legend to Figure 1 were analyzed for angiogenesis. Pimonidazole and CD-31 staining showed that positive spot area and positive stained vessels were increased in the iron-depleted condition. Scale bars: 50 mm. (*b*) MVD is increased in the iron-depleted condition. Data are means ± SD. Statistical significance (**) was determined as $p < 0.05$. (*c*) Western blot analysis of tumor-homogenized samples showed that VEGF and TfR-1 were upregulated in the iron-depleted condition. Similarly, HIF-1α was also upregulated at the nucleus protein level. Each tumor sample was obtained from three individual mice.

positive; G0 cycling stage cells were excluded. The Ki-67 labeling index revealed that an iron-deficient diet suppressed cancer cell proliferation compared to the normal diet group (Ki-67 labeling index: normal diet *vs.* iron-deficient diet = 0.211 ± 0.035 *vs.* 0.133 ± 0.032; $p = 0.0459$). Prussian blue staining was almost negative in the tissue in iron-deficient group.

### Iron depletion followed by hypoxia and angiogenesis

We hypothesized that iron depletion induced a reduction of serum hemoglobin and tissue hypoxia. Iron depletion also upregulates angiogenesis in the tumor. To test these hypotheses, we investigated pimonidazole and CD-31 staining (Fig. 2*a*). Tumor hypoxia was increased in the group fed an iron-deficient diet. CD-31 staining was performed to investigate whether iron depletion induced angiogenesis. Microvessel density (MVD) was calculated to count CD-31-positive vessels (Fig. 2*b*). CD-31-positive vessels were increased in an iron-depleted condition. The MVD of the iron-deficient diet group was higher than that of the normal diet group (MVD: normal diet *vs.* iron-deficient diet = 32.02 ± 25.24 *vs.* 64.96 ± 24.71; $p = 0.045439$). This result suggested that iron depletion induced angiogenesis via hypoxia.

### Angiogenesis was induced by iron depletion via HIF-1α upregulation

To identify the mechanism by which iron depletion induced angiogenesis *via* hypoxia, a Western blot analysis was performed using homogenized tissue samples. The expression of transferrin receptor 1 (TfR-1) was determined to confirm the effect of iron depletion in tumor tissue samples. As TfR-1

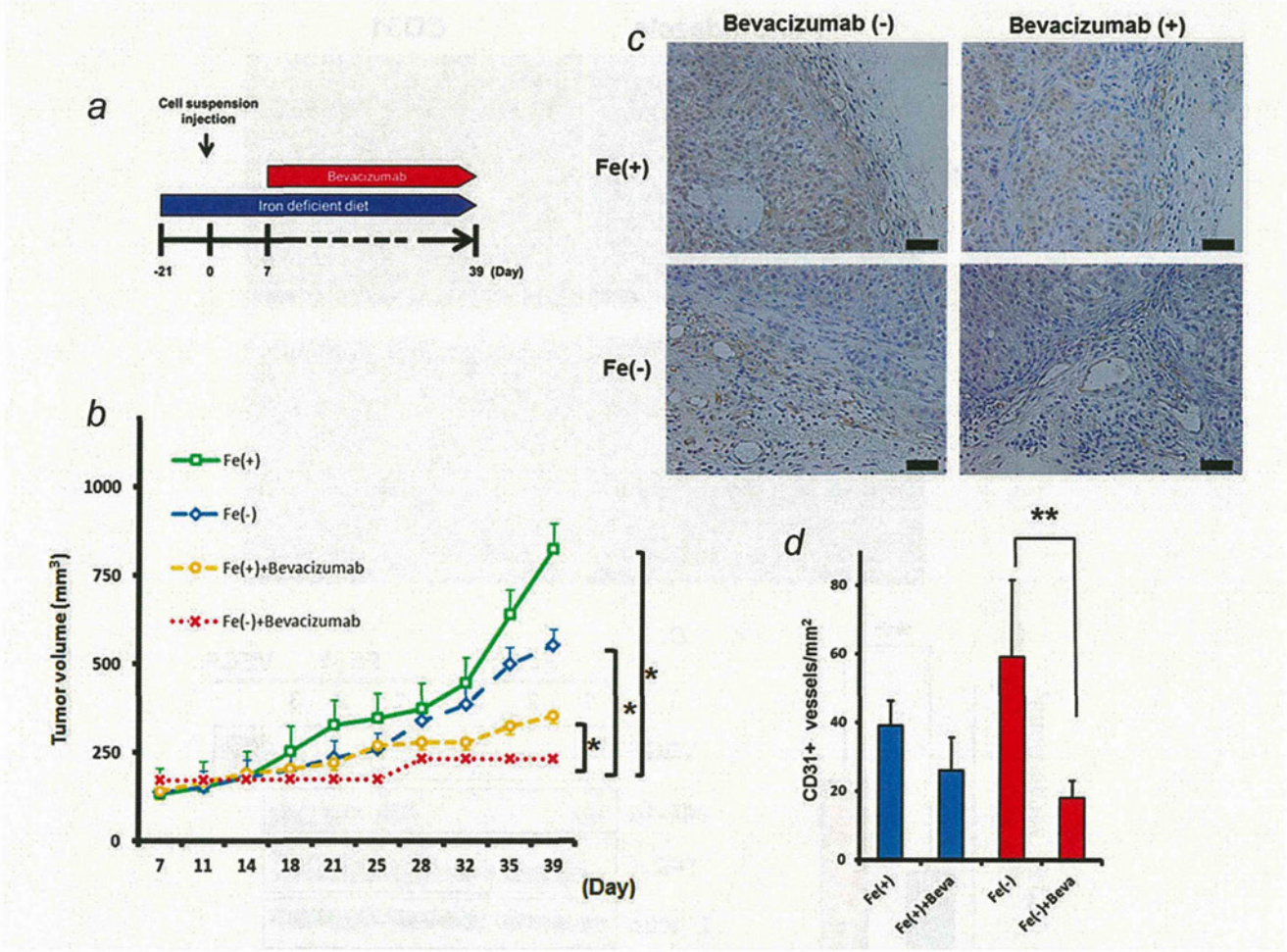


**Figure 3.** Bevacizumab synergistically suppressed tumor growth in an iron-depleted condition. (*a*) An iron-deficient diet was started 3 weeks before inoculating A549 cells on the backs of mice (day 21). The iron-deficient diet was continuously fed until the end of the study. (*b*) Bevacizumab (5 mg/kg) or saline as a control was administered ip twice/week. Tumor volume was measured as a cube (length × width × height) and was tracked up to 39 days. Five mice were used for each group. Tumor growth was expressed as mean tumor volume ± SD. Statistical significance (*) was determined as $p < 0.01$. Tumor growth was significantly inhibited in the combination group as compared to the control, bevacizumab or Fe (−) groups. (*c*) CD-31 staining revealed that positively stained vessels were increased in the iron-depleted condition. Scale bars: 50 mm. (*d*) Bevacizumab decreased MVD in both normal diet group and iron-deficient diet group.

expression changes based on the serum iron level, a decrease in serum iron levels increases TfR-1 expression.[19] Whole-cell lysate from homogenized tissue samples showed TfR-1 was upregulated in the iron-deficient diet group (Fig. 2*c*). Subsequently, the expression status of HIF-1α in nuclei was determined. HIF-1α is known to play a critical role in angiogenesis *via* hypoxia.[2,20] Western blot analysis of an extraction from nuclei showed the expression of HIF-1α in the iron-deficient diet group was higher than that of the normal group (Fig. 2*c*). This result suggested that iron depletion induced hypoxia *via* HIF-1α, which caused angiogenesis.

### Bevacizumab synergistically suppressed tumor growth by inhibiting upregulated angiogenesis

As shown above, we found that iron depletion was followed by hypoxia and angiogenesis. Thus, an antiangiogenic therapeutic agent (bevacizumab) was predicted to have a synergetic effect on suppressing tumor growth in an iron-depleted condition. Bevacizumab was administrated ip 5 mg/kg twice a week to mice with subcutaneous tumors fed either an iron-deficient or a normal diet. This dose and schedule were cited in the previous reports.[21,22] Bevacizumab had a synergistic effect on inhibiting tumor growth on Day 39 (tumor volume: normal diet [857.6 ± 129.0 $cm^3$], iron-deficient diet [401.8 ± 126.6 $cm^3$], normal diet + bevacizumab [221.6 ± 63.8 $cm^3$], iron-deficient diet + bevacizumab [61.0 ± 27.5 $cm^3$]) (Figs. 3*a* and 3*b*). To calculate MVD, CD-31 staining was performed (Fig. 3*c*). We could confirmed that bevacizumab inhibited angiogenesis in spite of induction by iron depletion condition (MVD: normal diet [39 ± 7.3], iron-deficient diet [59 ± 22.4], normal diet + bevacizumab [26 ± 9.7], iron-

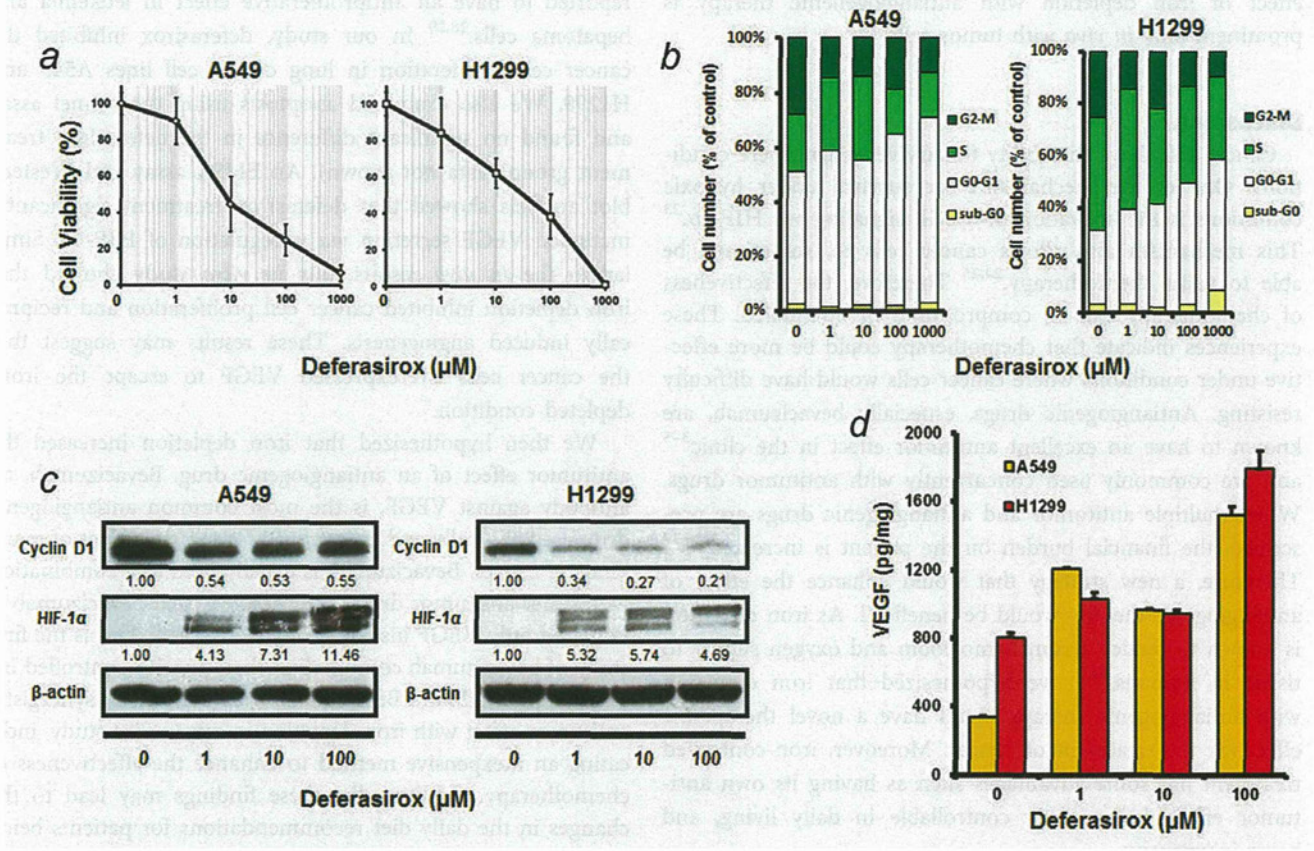


**Figure 4.** Iron depletion inhibited cell proliferation *via* cell-cycle arrest and induced VEGF secretion *in vitro*. (*a*) Cultured A549 cells and H1299 cells were treated with the indicated concentrations of deferasirox for 24 h and the cell viability was measured by the WST-1 method. (*b*) The cells were treated with different concentrations of deferasirox for 24 h and the cell-cycle distribution was analyzed by flow cytometry. Each histogram consists of the following four cell cycle populations; sub-G0 (black), G0-G1 (white), S (light gray) and G2-M (dark gray). (*c*) Whole-cell lysates and nuclear protein of these cells treated with the indicated concentrations of deferasirox were used for Western blot to determine its inhibitory effects on cell cycle and upregulation effects on HIF-1α. The expression level of each protein was calculated relative to its expression in mock-treated cells, whose expression level was designated as 1. (*d*) Supernatant treated with the indicated concentrations of deferasirox was harvested and VEGF secretion examined by ELISA.

deficient diet + bevacizumab [18 ± 5.1]) (Fig. 3*d*). None of the mice died owing to drug-induced toxicity and no other significant adverse events were observed.

### Iron depletion inhibited cell proliferation via cell-cycle arrest in vitro

To reproduce an iron-depleted condition *in vitro*, an iron chelator was used (deferasirox, Exjade™). Deferasirox suppressed cancer cell proliferation in A549 and H1299 cells in a dose-dependent manner (Fig. 4*a*). To identify the mechanism of inhibition, a flow cytometry analysis for cell-cycle distribution was performed (Fig. 4*b*). Deferasirox increased the population of the G0-G1 phase in the A549 and H1299 cell lines. To confirm the results of the flow cytometry analysis, Western blot analysis was performed using a total protein extraction of the A549 and H1299 cells. The Western blot showed that deferasirox decreased cyclin D1 in a dose-dependent manner (Fig. 4*c*). Taken together, these results suggest that iron depletion inhibited cancer cell proliferation *via* cell-cycle arrest *in vitro*.

### Iron depletion induced VEGF secretion in A549 and H1299 supernatant via upregulation of HIF-1α

To investigate whether iron depletion induces angiogenesis *via* HIF-1α, a Western blot analysis and ELISA assay were performed. Deferasirox treatment induced nuclear HIF-1α expression (Fig. 4*c*) and significantly increased VEGF secretion from A549 and H1299 cells, both in a dose-dependent manner (Fig. 4*d*). These results suggested that iron deficiency induced angiogenesis *via* HIF-1α and VEGF signaling. However, *in vitro* angiogenesis assay (tube formation assay) did not show the increase by deferasirox administration (Supporting Information Fig. S3). The reason was that deferasirox did not affect HUVEC in proliferation and VEGF secretion in the absence of tumor cells *in vitro*. Thus, the combination

effect of iron depletion with antiangiogenenic therapy is prominent only *in vivo* with tumor cells.

## Discussion

Cancer cells have the ability to survive under severe conditions. One of the mechanisms for survival under hypoxic conditions is the activation of VEGF signaling *via* HIF-1α.[23] This mechanism also allows cancer cells to, sometimes, be able to resist chemotherapy.[24,25] Therefore, the effectiveness of chemotherapy can be compromised or attenuated. These experiences indicate that chemotherapy could be more effective under conditions where cancer cells would have difficulty resisting. Antiangiogenic drugs, especially bevacizumab, are known to have an excellent antitumor effect in the clinic[3–5] and are commonly used concurrently with antitumor drugs. When multiple antitumor and antiangiogenic drugs are prescribed, the financial burden on the patient is increased.[26,27] Therefore, a new strategy that would enhance the effect of antiangiogenic therapy would be beneficial. As iron depletion is known to reduce serum hemoglobin and oxygen supply to tissue in humans,[10,11] we hypothesized that iron depletion with antiangiogenic therapy could have a novel therapeutic effect for the treatment of cancer. Moreover, iron-controlled treatment has some advantages such as having its own antitumor effect, being easily controllable in daily living, and being inexpensive.

First, we examined the effect of iron depletion on the mice and tumor growth. The iron-depleted mice revealed low serum levels of hemoglobin, iron, red blood cells and ferritin compared to the mice fed a normal diet. Tumor growth was suppressed in the iron-depleted mice. Tumor tissue was extracted and examined by histology and immunohistology. Iron deposits in the stroma of the tumors were reduced in the iron-depleted mice. This phenomenon suggested that the iron condition of the tumor influenced not only the cancer cell but also stroma cells. Pimonidazole (Hypoxyprobe-1 kit) and CD-31 staining showed that iron depletion induced hypoxia and angiogenesis. To confirm hypoxia in the tumor and analyze the differences in cell signaling, we further examined the expression of HIF-1α. HIF-1α was predictably upregulated in iron-depleted tumors at the protein level. Taken together, these results suggested that iron depletion suppressed tumor growth and reciprocally induced angiogenesis *via* hypoxia. To the best of our knowledge, there is no previous report of this reciprocal phenomenon.

We next investigated the mechanism of iron deficiency and reciprocally induced angiogenesis *in vitro*. We used an iron chelator (deferasirox) to stimulate iron depletion owing to its usefulness *in vitro* and the expectation to apply it clinically. Deferasirox is the first orally bioavailable iron chelator with an indication for the treatment of iron overload in transfusion-dependent anemias. Deferasirox is the most useful iron chelator in the clinical setting and has been reported to have an antiproliferative effect in leukemia and hepatoma cells.[28,29] In our study, deferasirox inhibited the cancer cell proliferation in lung cancer cell lines A549 and H1299. We also examined apoptosis using the tunnel assay and found no significant difference in the deferasirox treatment group (data not shown). An ELISA assay and Western blot analysis showed that deferasirox treatment significantly increased VEGF secretion *via* upregulation of HIF-1α. Similar to the *in vivo* results, our *in vitro* study showed that iron depletion inhibited cancer cell proliferation and reciprocally induced angiogenesis. These results may suggest that the cancer cells overexpressed VEGF to escape the iron-depleted condition.

We then hypothesized that iron depletion increased the antitumor effect of an antiangiogenic drug. Bevacizumab, an antibody against VEGF, is the most common antiangiogenic drug used clinically and is approved for the treatment of many kinds of cancer. Bevacizumab is usually used as a combination with other antitumor drug. The reason is that bevacizumab is targeting only VEGF instead of the cancer cell. This is the first study of bevacizumab combination therapy with controlled internal iron condition. Bevacizumab had a dramatic synergistic antitumor effect with iron depletion in our *in vivo* study, indicating an inexpensive method to enhance the effectiveness of chemotherapy. Additionally, these findings may lead to the changes in the daily diet recommendations for patients being treated with an antiangiogenic drug. Iron depletion condition induced antiproliferative effect and angiogenesis. As a result, bevacizumab inhibited angiogenesis and provided strong antitumor effect. Of course, the mechanism is not completely explained and further *in vivo* studies are necessary. For example, *in vivo* live imaging of the tumor growth as well as angiogenesis may be extremely useful.[30–34]

Bevacizumab is an established antiangiogenic drug with clinical benefits for many kinds of cancer.[35,36] However, there is no reliable biomarker or method by which curative effect can be predicted.[37,38] Our study showed that bevacizumab combined with iron depletion was very effective; therefore, we hypothesized that serum iron level could be a novel bevacizumab biomarker. We previously conducted a retrospective study to investigate the correlation between serum hemoglobin level and bevacizumab response rate in 34 patients with colorectal cancer in our facility assessed by RECIST criteria between September 2007 and July 2010.[39] Patient characteristics are summarized in Supporting Information Table 1. The response rate of the low-Hb patient group was higher than that of high-Hb group (41.2 *vs.* 17.6%). This result combined with the results of our present study suggests that a prospective study of bevacizumab with iron control therapy in patients with cancer is warranted.

## Conclusions

In conclusion, iron depletion inhibited the cancer cell proliferation and reciprocally induced angiogenesis *in vitro* and *in*

*vivo*. Bevacizumab had a dramatic synergistic antitumor effect with iron depletion. Treatment to create an iron-depleted condition could induce a novel therapeutic effect with antiangiogenic drugs in the treatment of cancer.

## Acknowledgements

The authors are grateful to Mr. Toru Tanida and Ms. Tae Yamanishi for their technical assistance and Dr. Oka and Dr. Miyazaki of Saiwaicho Hospital (Okayama, Japan) for useful discussions.

## References

1. Kim KJ, Li B, Winer J, et al. Inhibition of vascular endothelial growth factor-induced angiogenesis suppresses tumour growth in vivo. *Nature* 1993;362:841–4.
2. Forsythe JA, Jiang BH, Iyer NV, et al. Activation of vascular endothelial growth factor gene transcription by hypoxia-inducible factor 1. *Mol Cell Biol* 1996;16:4604–13.
3. Hurwitz H, Fehrenbacher L, Novotny W, et al. Bevacizumab plus irinotecan, fluorouracil, and leucovorin for metastatic colorectal cancer. *N Engl J Med* 2004;350:2335–42.
4. Kabbinavar FF, Hambleton J, Mass RD, et al. Combined analysis of efficacy: the addition of bevacizumab to fluorouracil/leucovorin improves survival for patients with metastatic colorectal cancer. *J Clin Oncol* 2005;23: 3706–12.
5. Saltz LB, Clarke S, Diaz-Rubio E, et al. Bevacizumab in combination with oxaliplatin-based chemotherapy as first-line therapy in metastatic colorectal cancer: a randomized phase III study. *J Clin Oncol* 2008;26:2013–19.
6. Richmond HG. Induction of sarcoma in the rat by iron-dextran complex. *Br Med J* 1959;1:947–9.
7. Okada S, Hamazaki S, Toyokuni S, et al. Induction of mesothelioma by intraperitoneal injections of ferric saccharate in male Wistar rats. *Br J Cancer* 1989;60: 708–11.
8. Kato J, Miyanishi K, Kobune M, et al. Long-term phlebotomy with low-iron diet therapy lowers risk of development of hepatocellular carcinoma from chronic hepatitis C. *J Gastroenterol* 2007;42: 830–6.
9. Hann HW, Stahlhut MW, Blumberg BS. Iron nutrition and tumor growth: decreased tumor growth in iron-deficient mice. *Cancer Res* 1988; 48:4168–70.
10. Becker A, Stadler P, Lavey RS, et al. Severe anemia is associated with poor tumor oxygenation in head and neck squamous cell carcinomas. *Int J Radiat Oncol Biol Phys* 2000;46: 459–66.
11. Vaupel P, Mayer A, Briest S, et al. Oxygenation gain factor: a novel parameter characterizing the association between hemoglobin level and the oxygenation status of breast cancers. *Cancer Res* 2003;63:7634–7.
12. Shirakawa Y, Naomoto Y, Kimura M, et al. Topological analysis of p21WAF1/CIP1 expression in esophageal squamous dysplasia. *Clin Cancer Res* 2000;6:541–50.
13. Chang YS, Adnane J, Trail PA, et al. Sorafenib (BAY 43-9006) inhibits tumor growth and vascularization and induces tumor apoptosis and hypoxia in RCC xenograft models. *Cancer Chemother Pharmacol* 2007;59:561–74.
14. Schmeding M, Rademacher S, Boas-Knoop S, et al. rHuEPo reduces ischemia-reperfusion injury and improves survival after transplantation of fatty livers in rats. *Transplantation* 2010;89: 161–8.
15. Fei J, Hong A, Dobbins TA, et al. Prognostic significance of vascular endothelial growth factor in squamous cell carcinomas of the tonsil in relation to human papillomavirus status and epidermal growth factor receptor. *Ann Surg Oncol* 2009;16:2908–17.
16. Myoung H, Hong SD, Kim YY, et al. Evaluation of the anti-tumor and anti-angiogenic effect of paclitaxel and thalidomide on the xenotransplanted oral squamous cell carcinoma. *Cancer Lett* 2001;163:191–200.
17. Hashimoto Y, Watanabe Y, Shirakiya Y, et al. Establishment of biological and pharmacokinetic assays of telomerase-specific replication-selective adenovirus. *Cancer Sci.* 2008;99:385–90.
18. Ohara T, Takaoka M, Toyooka S, et al. Inhibition of mTOR by temsirolimus contributes to prolonged survival of mice with pleural dissemination of non-small-cell lung cancer cells. *Cancer Sci* 2011;102:1344–9.
19. Kohgo Y, Niitsu Y, Kondo H, et al. Serum transferrin receptor as a new index of erythropoiesis. *Blood* 1987;70:1955–8.
20. Ke Q, Costa M. Hypoxia-inducible factor-1 (HIF-1). *Mol Pharmacol* 2006;70:1469–80.
21. Schicher N, Paulitschke V, Swoboda A, et al. Erlotinib and bevacizumab have synergistic activity against melanoma. *Clin Cancer Res* 2009; 15:3495–3502.
22. Argov M, Kashi R, Peer D, et al. Treatment of resistant human colon cancer xenografts by a fluoxetine-doxorubicin combination enhances therapeutic responses comparable to an aggressive bevacizumab regimen. *Cancer Lett* 2009;274:118–25.
23. Shima DT, Deutsch U, D'Amore PA. Hypoxic induction of vascular endothelial growth factor (VEGF) in human epithelial cells is mediated by increases in mRNA stability. *FEBS Lett* 1995;370: 203–8.
24. Guminski AD, Harnett PR, deFazio A. Scientists and clinicians test their metal-back to the future with platinum compounds. *Lancet Oncol* 2002;3: 312–8.
25. Chang A. Chemotherapy, chemoresistance and the changing treatment landscape for NSCLC. *Lung Cancer* 2011;71:3–10.
26. Tappenden P, Jones R, Paisley S, et al. The cost-effectiveness of bevacizumab in the first-line treatment of metastatic colorectal cancer in England and Wales. *Eur J Cancer* 2007;43: 2487–94.
27. Montero AJ, Avancha K, Gluck S, et al. A cost-benefit analysis of bevacizumab in combination with paclitaxel in the first-line treatment of patients with metastatic breast cancer. *Breast Cancer Res Treat* 2012;132: 747–51.
28. Ohyashiki JH, Kobayashi C, Hamamura R, et al. The oral iron chelator deferasirox represses signaling through the mTOR in myeloid leukemia cells by enhancing expression of REDD1. *Cancer Sci* 2009;100:970–77.
29. Lescoat G, Chantrel-Groussard K, Pasdeloup N, et al. Antiproliferative and apoptotic effects in rat and human hepatoma cell cultures of the orally active iron chelator ICL670 compared to CP20: a possible relationship with polyamine metabolism. *Cell Prolif* 2007;40:755–67.
30. Hoffman, RM. Orthotopic metastatic mouse models for anticancer drug discovery and evaluation: a bridge to the clinic. *Invest New Drugs* 1999;17:343–59.
31. Hoffman, RM. The multiple uses of fluorescent proteins to visualize cancer in vivo. *Nat Rev Cancer* 2005;5:796–806.
32. Hoffman RM, Yang M. Color-coded fluorescence imaging of tumor-host interactions. *Nat Protoc* 2006;1:928–35.
33. Amoh Y, Yang M, Li L, et al. Nestin-linked green fluorescent protein transgenic nude mouse for imaging human tumor angiogenesis. *Cancer Res* 2005;65:5352–7.
34. Amoh Y, Li L, Tsuji K, et al. Dual-color imaging of nascent blood vessels vascularizing pancreatic cancer in an orthotopic model demonstrates antiangiogenesis efficacy of gemcitabine. *J Surg Res* 2006;132:164–9.
35. Shih T, Lindley C. Bevacizumab: an angiogenesis inhibitor for the treatment of solid malignancies. *Clin Ther* 2006;28:1779–1802.
36. Wheatley-Price P, Shepherd FA. Targeting angiogenesis in the treatment of lung cancer. *J Thorac Oncol* 2008;3:1173–84.
37. Jubb AM, Harris AL. Biomarkers to predict the clinical efficacy of bevacizumab in cancer. *Lancet Oncol* 2010;11:1172–83.
38. Mancuso A, Sternberg CN. Colorectal cancer and antiangiogenic therapy: what can be expected in clinical practice?*Crit Rev Oncol Hematol* 2005;55: 67–81.
39. Eisenhauer EA, Therasse P, Bogaerts J, et al. New response evaluation criteria in solid tumours: revised RECIST guideline (version 1.1). *Eur J Cancer* 2009;45:228–47.